

On the dynamics of overshooting convection in spherical shells: Effect of density stratification and rotation

LYDIA KORRE¹ AND NICHOLAS A. FEATHERSTONE²

¹*Laboratory for Atmospheric and Space Physics, Boulder, CO 80303, USA*

²*Southwest Research Institute, Department of the Space Studies, Boulder, CO 80302, USA*

ABSTRACT

Overshooting of turbulent motions from convective regions into adjacent stably stratified zones plays a significant role in stellar interior dynamics as this process may lead to mixing of chemical species, and contribute to the transport of angular momentum and magnetic fields. We present a series of fully non-linear, three-dimensional (3D) anelastic simulations of overshooting convection in a spherical shell which are focused on the dependence of the overshooting dynamics on the density stratification and the rotation, both key ingredients in stars which however have not been studied systematically together via global simulations. We demonstrate that the overshoot lengthscale is not simply a monotonic function of the density stratification in the convective region but instead, it depends on the ratio of the density stratifications in the two zones. Additionally, we find that the overshoot lengthscale decreases with decreasing Rossby number Ro and scales as $Ro^{0.23}$ while it also depends on latitude with higher Rossby cases leading to a weaker latitudinal variation. We examine the mean flows arising due to rotation and find that they extend beyond the base of the convection zone into the stable region. Our findings may provide a better understanding of the dynamical interaction between stellar convective and radiative regions, and motivate future studies particularly related to the solar tachocline and the implications of its overlapping with the overshoot region.

1. INTRODUCTION

The dynamical interaction of convectively unstable zones (CZ) with stably stratified radiative zones (RZ) has been a crucial yet still poorly understood problem in the astrophysical context, despite the fact that such regions exist side-by-side in almost every star and across many evolutionary phases. The boundaries between such stellar regions are not impenetrable, allowing turbulent convective motions generated in the convectively unstable layer to travel into the adjacent stable regions through inertia. This process, termed “overshooting”, has substantial implications for stellar evolution as it can lead to changes in stellar surface element abundances and differential rotation through the mixing of chemical species and the transport of angular momentum (see e.g., [Pinsonneault 1997](#); [Baraffe et al. 2017](#)). It may also alter the thermal stratification of the radiative zone, converting a portion of it into an adiabatic region that forms an extended CZ, in which case the process is usually termed “penetration” ([Zahn et al. 1982](#); [Zahn 1991](#)). Furthermore, overshooting can advect magnetic fields from the CZ into the RZ via turbulent pumping (see e.g., [Tobias et al. 2001](#); [Korre et al. 2021](#)), and may lead to the establishment of an interface dynamo at the base of the solar convection zone ([Parker 1993](#); [Charbonneau & MacGregor 1997](#)).

1.1. *Previous Studies of Non-rotating Overshooting/Penetrative Convection*

There exists a large body of astrophysical literature on the topic of convective overshooting. Early studies were performed using modal expansions (e.g., [Latour et al. 1976](#); [Toomre et al. 1976](#); [Latour et al. 1981](#)) or within the context of mixing-length theory (see, for instance [Shaviv & Salpeter 1973](#); [Maeder 1975](#)). However, as discussed in [Renzini \(1987\)](#), there were many inconsistencies among the results of the mixing-length theory studies due to their sensitivity to the underlying model assumptions. As a result, convective overshooting research came to rely on alternative, more sophisticated approaches, ranging from early modal-expansion models to modern, fully non-linear computational models. These studies have been mainly focused on (1) the variation of the lengthscales associated with the overshooting motions in response to stellar parameters/properties and (2) the degree to which overshooting convection modifies the stable background stratification (thermal mixing) and the parameters under which it manages to turn part of it into an adiabatic layer (penetrative convection).

Early work focused on penetrative convection was performed by [Zahn et al. \(1982\)](#), who employed a modal expansion approach to study overshooting in a Boussinesq system and found substantial penetration within the stable region. The effects of background density stratification were later included in the study of [Massaguer et al. \(1984\)](#) who demonstrated that increasing stratification in the CZ may lead to larger penetration lengthscales due to the enhanced flow asymmetries arising from compressibility effects. Scaling arguments have also been applied, as in [Zahn \(1991\)](#) who identified two dynamical regimes of interest below the base of the convective region: a penetrative layer for high Péclet numbers and a thermal adjustment (overshoot) layer for low Péclet numbers (where the Péclet number characterizes the strength of thermal advection relative to thermal diffusion). The existence of these two regimes was subsequently confirmed through the application of 2D, fully non-linear simulations carried out in Cartesian and cylindrical geometries (e.g., [Hurlburt et al. 1986, 1994](#); [Rogers & Glatzmaier 2005](#); [Rogers et al. 2006](#)).

One of the first systematic studies of overshooting/penetrative convection via fully non-linear simulations was that of [Hurlburt et al. \(1994\)](#) (also see [Hurlburt et al. 1986](#)) who performed 2D Cartesian compressible calculations. That study explored the dependence of overshooting on the so-called stiffness parameter, a measure of the degree of relative stability of the RZ compared with the CZ. It also identified two scaling regimes, consistent with the findings of [Zahn \(1991\)](#), and showed that the penetrative regime was associated with lower stiffness parameters and larger penetration depths while the overshoot regime was related to higher stiffness parameters and possessed smaller overshoot lengthscales.

These results have largely been confirmed within the context of fully non-linear 3D simulations. Studies carried out in both Cartesian and spherical geometries have demonstrated that the overshoot lengthscale decreases with increasing stiffness parameter ([Brummell et al. 2002](#); [Korre et al. 2019](#)). However, as noted in [Korre et al. \(2019\)](#), the transition width between the CZ and the RZ also appears to play an important role in determining the amount of overshooting below the base of the convective region. Interestingly, these 3D studies did not identify pure penetration, namely the extension of the CZ further down into the stable RZ, but instead, they only observed partial thermal mixing in the RZ, associated with the stronger downflows.

This lack of pure penetration may be attributed to the lower filling factor of the plumes for 3D simulations relative to 2D simulations when run in otherwise similar parameter regimes (for more on this, see e.g., [Brummell et al. 2002](#); [Rempel 2004](#)). It may also result from the tendency of the overshoot lengthscale and degree of penetration to be established by strongest downflows (see e.g., [Pratt et al. 2017](#); [Korre et al. 2019](#)). Both the strength of these downflows and the Péclet numbers achieved in simulations are explicitly dependent on the degree of thermal forcing as expressed through a Rayleigh number. The dependence of the overshoot lengthscale on the Rayleigh number has been explored in several studies (see [Brummell et al. 2002](#); [Rogers & Glatzmaier 2005](#); [Korre et al. 2019](#)), but different scalings were observed, possibly due to the different set-up configurations, geometries, and boundary conditions. Large density stratification, which enhances the asymmetry between upflows and downflows, may also lead to stronger overshooting and eventually an adiabatic penetrative layer within the RZ. This effect was discussed in [Massaguer et al. \(1984\)](#), but has yet to be investigated systematically via fully non-linear, 3D global simulations.

1.2. *The Effects of Rotation*

Relatively few studies have explicitly examined the response of overshooting to the presence of rotation. While the details vary, these studies suggest that the overshooting depth δ decreases with decreasing Rossby number Ro (where Ro expresses the relative strength of inertial to Coriolis forces). Cartesian studies carried out in a rotating f -plane by [Brummell et al. \(2002\)](#) found that, for a limited range of Ro , $\delta \propto Ro^{0.15}$. Similar results were reported by [Pal et al. \(2007\)](#) who found that $\delta \propto Ro^{0.2}$ at the poles and $\delta \propto Ro^{0.4}$ at mid-latitudes. [Augustson & Mathis \(2019\)](#) recently

presented a model of rotating overshooting convection which employs the semi-analytical model of Zahn (1991) and estimated the scaling of the overshoot depth with the Rossby number. They also found that δ decreases with decreasing Rossby number like $\delta \propto \text{Ro}^{0.3}$.

Overshooting in the Sun is thought to play a role in many aspects of the global flows and magnetic fields. For instance, temperature variations arising from rotating convective overshoot are thought to be responsible for inducing a thermal wind in the convection zone that leads to the observed tilt of differential rotation contours (Kitchatinov & Ruediger 1995; Rempel 2005; Miesch et al. 2006; Howe 2009). Moreover, overshooting may pump magnetic field into the solar tachocline region where it can be stretched into large-scale toroidal field. As a result, the tachocline has been the presumed seat of the solar dynamo for some time, figuring particularly prominently in the flux-transport and interface class of dynamo models (e.g., Parker 1993; Dikpati & Charbonneau 1999; Rempel 2006).

For these reasons, a region of overshoot has been included in several 3D models of stellar convection. This includes studies within the solar context (e.g., Ghizaru et al. 2010; Racine et al. 2011; Brun et al. 2011; Guerrero et al. 2013, 2016; Augustson et al. 2015), as well as others related to more massive stars (e.g., Browning et al. 2004; Brun et al. 2005; Featherstone et al. 2009; Augustson et al. 2012, 2016). Throughout those studies, however, the region of overshoot was but one ingredient in numerical experiments targeting other aspects of the convection and its resulting dynamo. For instance, Brun et al. (2017) studied solar-like overshooting convection but mostly focused on the mean flows arising within different rotational regimes and the dependence of overshooting on stellar mass (also see Brun et al. 2011; Augustson et al. 2012). A systematic study of the effects of rotation on the convective overshooting dynamics, however, has yet to be performed in 3D global numerical calculations.

In this work, we use fully non-linear 3D models of stratified convection in a spherical shell geometry to examine the dependence of convective overshooting on strong density stratification. We also develop scaling laws that describe the overshoot lengthscale with Rossby number and investigate the properties of angular momentum transport and meridional flow in the coupled CZ-RZ system. The paper is organized as follows. In Section 2, we describe our two-layered model formulation and provide the set of anelastic Navier-Stokes equations along with the initial conditions, and the boundary conditions used in our simulations. In Section 3, we present our results associated with the effect of the density stratification on the non-rotating overshooting dynamics. In Section 4, we study the dynamics related to the effect of rotation on the turbulent convective overshooting motions, as well as the dependence of the overshoot lengthscale on the Rossby number and on latitude. In Section 5, we focus on the rotational profiles arising at different Rossby numbers, the associated mean flows and the angular momentum transport and balances within the convection zone and the overshoot region. Finally, in Section 6, we summarize our results, provide comparisons with previous work, and discuss the implications of these results in the solar context.

2. MODEL FORMULATION

2.1. Dimensional Equations

We aim to explore the dynamics associated with a two-zone system that consists of a convectively unstable region that lies above a stably stratified radiative zone. For all cases presented in this work, we use a fixed aspect ratio $r_i/r_o = 0.45$ where r_i is the inner radius and r_o is the outer radius of the spherical shell. Also, we assume that the convective region has a fixed depth $L = r_o - r_c = 0.2408r_o$, where $r_c = 0.7592r_o$ is the radius at the bottom of the CZ. Our chosen depth L corresponds to the solar convection zone from $\sim 0.7187R_\odot$ to $\sim 0.9467R_\odot$, hence only accounting for its inner part and not the outer layers where radiative transfer processes take place. We are interested in the dynamics within deep stellar interiors where the flows are subsonic. As such, we employ the anelastic approximation which filters out the sound waves and assumes small perturbations of the thermodynamic variables compared with their mean (Gough 1969; Gilman & Glatzmaier 1981). Therefore, we solve the 3D Navier-Stokes equations under the anelastic and Lantz-Braginsky-Roberts approximations (Lantz 1992; Braginsky & Roberts 1995), the latter of which is exact in the convection zone where the reference state is adiabatic.

Then, the dimensional Navier-Stokes equations become

$$\frac{\partial \mathbf{u}}{\partial t} + \mathbf{u} \cdot \nabla \mathbf{u} + 2\Omega_o \hat{\mathbf{z}} \times \mathbf{u} = \frac{g(r)}{c_p} S \hat{\mathbf{r}} - \nabla(P/\bar{\rho}) + \frac{1}{\bar{\rho}} \nabla \cdot \mathbf{D}, \quad (1)$$

$$\nabla \cdot (\bar{\rho} \mathbf{u}) = 0, \quad (2)$$

$$\bar{\rho}\bar{T}\left(\frac{\partial S}{\partial t} + \mathbf{u} \cdot \nabla S + u_r \frac{d\bar{S}}{dr}\right) = \nabla \cdot (\bar{\rho}\bar{T}\kappa\nabla S) + Q + \Phi, \quad (3)$$

where $\mathbf{u} = (u_r, u_\theta, u_\phi)$ is the velocity field, P is the pressure, $\bar{\rho}$ is the reference density, \bar{T} is the reference temperature, $d\bar{S}/dr$ is the background entropy gradient, S characterizes the entropy perturbations about the reference state, Ω_o is the frame rotation rate, $g(r)$ is the gravity (where $g \propto 1/r^2$), and c_p is the specific heat at constant pressure. The viscosity ν and the thermal diffusivity κ are kept constant for simplicity. The viscous stress tensor \mathbf{D} is given by

$$\mathbf{D} = 2\bar{\rho}\nu(e_{ij} - \frac{1}{3}\nabla \cdot \mathbf{u}), \quad (4)$$

and the viscous heating is denoted by

$$\Phi = 2\bar{\rho}\nu[e_{ij}e_{ij} - \frac{1}{3}(\nabla \cdot \mathbf{u})^2], \quad (5)$$

where e_{ij} is the strain rate tensor. The internal heating term Q is proportional to the pressure such that $L_\odot = 4\pi \int_{r_i}^{r_o} Q(r)r^2 dr$, where L_\odot is the solar luminosity. As noted in Featherstone & Hindman (2016a), this profile is similar in structure to the one established in Model S (see e.g., Christensen-Dalsgaard et al. 1996). We taper the profile using a tanh function below the base of the CZ such that

$$Q(r) \propto \frac{1}{2} \left(\tanh\left(\frac{r-r_c}{0.01r_c}\right) + 1 \right) (\bar{P}(r) - \bar{P}(r_o)), \quad (6)$$

where \bar{P} is the reference pressure. It satisfies $Q(r) = -\nabla \cdot F_{rad}$, where F_{rad} is the radiative flux in the system given by

$$F_{rad}(r) = \frac{1}{r^2} \int_r^{r_o} Q(r')r'^2 dr'. \quad (7)$$

To close the set of equations (1)-(3), we use an equation of state given by

$$\frac{\rho}{\bar{\rho}} = \frac{P}{\bar{P}} - \frac{T}{\bar{T}} = \frac{P}{\gamma\bar{P}} - \frac{S}{c_p}, \quad (8)$$

assuming the ideal gas law

$$\bar{P} = \Re\bar{\rho}\bar{T}, \quad (9)$$

where $\rho(T)$ are the density (temperature) perturbations about the reference state, \Re is the gas constant, and $\gamma = c_p/c_v$ is the heat capacity ratio (where c_v is the specific heat at constant volume).

To create our two-layered system, we can then select an appropriate $d\bar{S}/dr$ profile that satisfies an adiabatic polytropic solution with $\gamma = 5/3$ in the convective region $r_c \leq r \leq r_o$ and which smoothly transitions to a stably stratified region for $r_i \leq r < r_c$. We note however, that there are more sophisticated approaches where the two-zone system can be created by assuming that the radiative heat flux depends on a varying (in density and temperature) thermal conductivity profile based on either computed and tabulated opacities or on approximations such as Kramers law (see e.g., Käpylä 2019; Käpylä et al. 2019; Viviani & Käpylä 2021).

We also specify the number of density scale-heights in the convection zone through $N_\rho = \ln(\bar{\rho}(r_c)/\bar{\rho}(r_o))$ (see Appendix A). Then, we integrate $d\bar{S}/dr$ from r_c inward, yielding a solution for \bar{S} . The integration constant is computed by matching the solution to the value of \bar{S} at the base of the CZ.

Using the fact that the entropy for a monatomic ideal gas is $\bar{S} = \ln(\bar{P}^{1/\gamma}/\bar{\rho})$, differentiating the latter with respect to the radius, and applying the hydrostatic balance equation $\partial\bar{P}/\partial r = -\bar{\rho}g$ we obtain

$$\frac{\bar{\rho}}{c_p} \frac{d\bar{S}}{dr} + \frac{g}{\gamma} \exp(-\gamma\bar{S}/c_p) \bar{\rho}^{(2-\gamma)} + \frac{d\bar{\rho}}{dr} = 0, \quad (10)$$

which we can solve numerically for the reference density profile $\bar{\rho}(r)$ given any background entropy gradient profile.

2.2. Non-dimensional Equations

We non-dimensionalize equations (1)-(3) using the depth of the convection zone $[l] = L$ as the lengthscale, the viscous timescale $[t] = L^2/\nu$, and the velocity scale $[u] = \nu/L$. Throughout the paper, we define the volume average of a quantity $q(r, \theta, \phi)$ in the CZ as

$$q_{cz} = \frac{\int_{r_c}^{r_o} \int_0^{2\pi} \int_0^\pi q r^2 \sin \theta d\theta d\phi dr}{\int_{r_c}^{r_o} \int_0^{2\pi} \int_0^\pi r^2 \sin \theta d\theta d\phi dr}. \quad (11)$$

For the density and temperature scales, we choose $[\rho] = \bar{\rho}_{cz}$, and $[T] = \bar{T}_{cz}$, respectively.

For the entropy perturbations S , we adopt a scaling related to the thermal energy flux F such that $[S] = LF_{cz}/(\bar{\rho}_{cz}\bar{T}_{cz}\kappa)$, where $F(r) = \int_{r_i}^r Q(r')r'^2 dr'/r^2$. We specify our chosen non-dimensional $d\bar{S}/dr$ profile in the RZ such that

$$\frac{d\bar{S}}{dr} = \frac{A}{2} \left(1 - \tanh \left(\frac{r - r_b}{d} \right) \right), \quad (12)$$

where $A = 10$, $r_b = 0.6453r_o$ and $d = 0.0456r_o$.

The non-dimensional gravity (reference density $\bar{\rho}$, reference temperature \bar{T}) is equivalent to the dimensional gravity (reference density, reference temperature) divided by g_{cz} ($\bar{\rho}_{cz}$, \bar{T}_{cz}). All the quantities are now non-dimensional and the non-dimensional anelastic Navier-Stokes equations become

$$\frac{\partial \mathbf{u}}{\partial t} + \mathbf{u} \cdot \nabla \mathbf{u} + \frac{2}{\text{Ek}} \hat{z} \times \mathbf{u} = \frac{\text{Ra}}{\text{Pr}} g(r) S \hat{\mathbf{r}} - \nabla(P/\bar{\rho}) + \frac{1}{\bar{\rho}} \nabla \cdot \mathbf{D}, \quad (13)$$

$$\nabla \cdot (\bar{\rho} \mathbf{u}) = 0, \quad (14)$$

$$\bar{\rho} \bar{T} \left(\frac{\partial S}{\partial t} + \mathbf{u} \cdot \nabla S + u_r \frac{d\bar{S}}{dr} \right) = \frac{1}{\text{Pr}} \nabla \cdot (\bar{\rho} \bar{T} \nabla S) + \frac{1}{\text{Pr}} Q_{nd} + \frac{\text{DiPr}}{\text{Ra}} \Phi, \quad (15)$$

where $Q_{nd} = LQ/F_{cz}$ is the non-dimensional internal heating function. In Fig. 1, we show the profile of $Q_{nd}(r)$ against r/r_o for the run with $N_\rho = 3$.

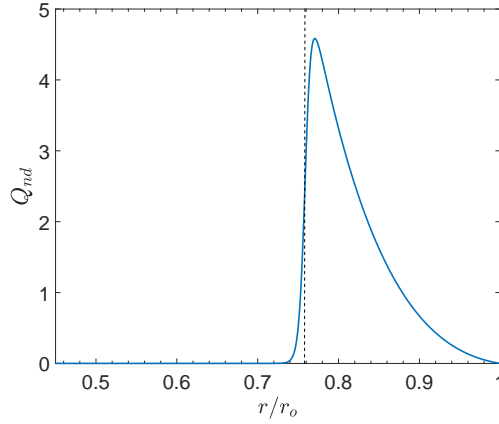


Figure 1. Profile of the non-dimensional heating function Q_{nd} against the radius r/r_o for the case with $N_\rho = 3$. The black dashed vertical line corresponds to the base of the convective region.

We now have four non-dimensional numbers: the flux Rayleigh number Ra , the Prandtl number Pr , the Ekman number Ek and the dissipation number Di , which are defined respectively as

$$\text{Ra} = \frac{g_{cz} F_{cz} L^4}{c_p \bar{\rho}_{cz} \bar{T}_{cz} \kappa^2 \nu}, \quad \text{Pr} = \frac{\nu}{\kappa}, \quad \text{Ek} = \frac{\nu}{\Omega_o L^2}, \quad \text{and} \quad \text{Di} = \frac{g_{cz} L}{c_p \bar{T}_{cz}}. \quad (16)$$

Note that, unlike Ra , Pr and Ek , Di is not a free parameter. It depends on the chosen N_ρ and accounts for the fact that we have two energy scales – a thermal scale and a kinetic scale. Thus, Di appears in the thermal equation to account for the viscous heating term, which is kinetic in nature.

We have run a series of 3D numerical simulations solving equations (13)-(15) using the Rayleigh code (Featherstone & Hindman 2016a; Matsui et al. 2016; Featherstone 2018) with a chosen non-dimensional background entropy gradient $d\bar{S}/dr$ as described above and shown in Figure 2.

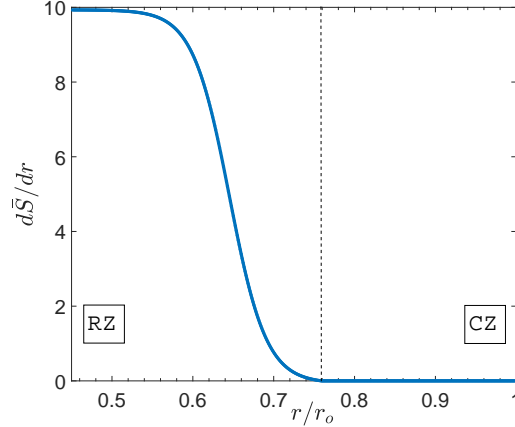


Figure 2. Profile of the non-dimensional background entropy gradient $d\bar{S}/dr$ versus r/r_o . The black dashed vertical line corresponds to the base of the convective region.

We use impenetrable and stress-free boundary conditions for the velocity. For the entropy perturbations, we assume $\partial S/\partial r|_{r_i} = 0$ at the inner boundary to account for the fixed flux of energy generated due to the nuclear burning at the stellar core while we fix the entropy at the outer boundary such that $S|_{r_o} = 0$. We note, however, that recent studies seem to suggest that a fixed flux outer boundary condition might also be a sensible choice in the stellar context (Matilsky et al. 2020). In all simulations, we assume a fixed $Pr = 1$ in order to avoid the onset of non-physical modes known to arise in rapidly rotating anelastic convective systems for $Pr < 1$ (e.g., Calkins et al. 2015), while we vary N_ρ , Ra and Ek (see Table 1). Each simulation is evolved from a zero initial velocity and small-amplitude perturbations in the entropy field until a statistically stationary and thermally relaxed state is reached.

3. EFFECT OF DENSITY STRATIFICATION ON THE NON-ROTATING OVERSHOOTING DYNAMICS

We begin by exploring the effect of the density stratification in the CZ quantified by N_ρ on the overshooting dynamics in a non-rotating spherical shell. In Fig. 3, we present snapshots of meridional slices of the radial velocity u_r at $Ra = 10^5$ for increasing values of N_ρ , ranging from $N_\rho = 0.01$ to $N_\rho = 4$. From a visual inspection, we see that, in all of these cases, the convective motions generated in the unstable CZ do not stop at the bottom of the CZ (marked by the inner black line), but they travel some distance into the stable RZ which does seem to depend on N_ρ , at least qualitatively. Furthermore, we notice that for increasing values of N_ρ , the velocity field becomes more asymmetrical with narrower lanes of downflows and wider lanes of upflows. This enhanced asymmetry is a result of the corresponding increased density stratification in the CZ. By contrast, as $N_\rho \rightarrow 0$, we are approaching the Boussinesq approximation limit, where the density is almost constant throughout the shell. Thus, the asymmetry for lower values of N_ρ is mostly a result of the sphericity and the mixed thermal boundary conditions (e.g., Korre et al. 2017), though Anders et al. (2020) recently showed that the latter do not substantially break the symmetry in the bulk of the convective region.

There are many different ways of examining quantitatively how far these convective motions can overshoot into the stable region. In this work we will rely on the radial variation of the kinetic energy to estimate overshooting lengthscales. Throughout the paper, we define the time and spherical average of a quantity q as

$$\tilde{q}(r) = \frac{1}{4\pi(t_2 - t_1)} \int_{t_1}^{t_2} \int_0^{2\pi} \int_0^\pi q(r, \theta, \phi, t) \sin \theta d\theta d\phi dt, \quad (17)$$

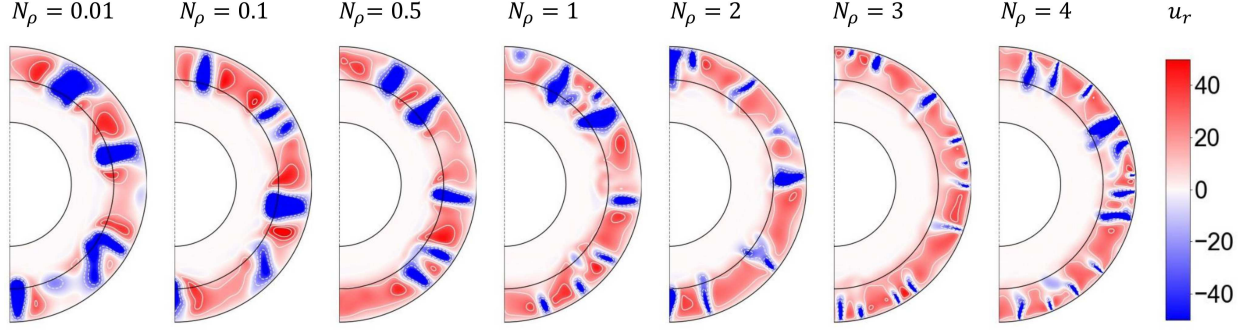


Figure 3. Snapshots of meridional slices of the radial velocity u_r at a selected longitude for different values of N_ρ (indicated above each panel) at $Ra = 10^5$ for the non-rotating runs. The inner black line marks the bottom of the convective region. The convective motions overshoot into the stable region in all N_ρ cases and the amount of overshooting depends on N_ρ .

and the time and azimuthal average of a quantity q as

$$\langle q(r, \theta) \rangle = \frac{1}{2\pi(t_2 - t_1)} \int_{t_1}^{t_2} \int_0^{2\pi} q(r, \theta, \phi) d\phi dt, \quad (18)$$

where $t_2 - t_1$ is a time interval in the simulation in a statistically stationary and thermally equilibrated state.

In Figure 4a, we plot the time- and spherically- averaged kinetic energy $\tilde{E}_k(r)$ (where $\tilde{E}_k(r) = (1/2)\bar{\rho}(\tilde{u}_r^2 + \tilde{u}_\theta^2 + \tilde{u}_\phi^2)$) for different N_ρ values at $Ra = 10^5$. We verify what we noticed in Fig. 3, namely that $\tilde{E}_k(r)$ is large in the CZ, but there is also substantial kinetic energy below the base of the convective region, where the convective motions overshoot. However, these motions do decelerate within the stable RZ, where they are no longer buoyantly driven there, and \tilde{E}_k decreases accordingly. We notice that \tilde{E}_k acquires a half-Gaussian profile below r_c , similarly to what Korre et al. (2019) recently found in their Boussinesq convective overshooting spherical shell simulations. Indeed, this seems to be a salient characteristic of the overshooting dynamics, independent of the approximation (here we assume the anelastic approximation) and the model set-up employed. Using this feature, we fit a Gaussian function of the form

$$f_G(r) = A_E \exp \left(- \left(\frac{r - r_c}{\sqrt{2}\delta_{Gf}} \right)^2 \right) \quad (19)$$

to the $\tilde{E}_k(r)$ data from the bottom of the CZ r_c down to the point where $\tilde{E}_k(r)$ is well-fit by Eq. (19) and use the computed width of this Gaussian $\delta_G = \delta_{Gf}/r_o$ as an estimate of how far the turbulent convective motions overshoot in the stable region, in an average sense (see for details Korre et al. 2019). In Figure 4b, we plot $\tilde{E}_k(r)$ for a typical run (with $N_\rho = 3$) along with the fitted function $f_G(r)$ given in Eq. (19) to illustrate how well a Gaussian of this form actually fits the numerical data with $\delta_G = 0.049$ for this case.

In order to examine the dependence of the overshooting lengthscale on the density stratification, in Fig. 5, we plot δ_G against N_ρ and notice that δ_G increases with increasing N_ρ for $N_\rho \lesssim 0.7$, while it starts decreasing with increasing N_ρ for $N_\rho > 0.7$. This result might initially seem counter-intuitive, since we would expect that the enhanced asymmetry, which leads to narrower downflows for larger values of N_ρ (as also seen in Fig. 3), would result in larger values of δ_G (see for instance Massaguer et al. 1984). However, it is crucial to also consider the density stratification in the RZ which is not the same for the different N_ρ cases in our simulations. We found that the relevant quantity is the ratio of the density stratification in the RZ over the one in the CZ, given by

$$R_\rho = \frac{(\bar{\rho}(r_i)/\bar{\rho}(r_c))}{(\bar{\rho}(r_c)/\bar{\rho}(r_o))}, \quad (20)$$

and not solely N_ρ . In Figure 6a, we plot the computed δ_G against R_ρ and find that δ_G decreases with decreasing R_ρ such that $\delta_G \propto R_\rho^{0.36}$. This indicates that R_ρ is a more sensible parameter for explaining our results. Indeed, the density ratio in the CZ is explicitly associated with both the degree of asymmetry of the flow and the strength of the

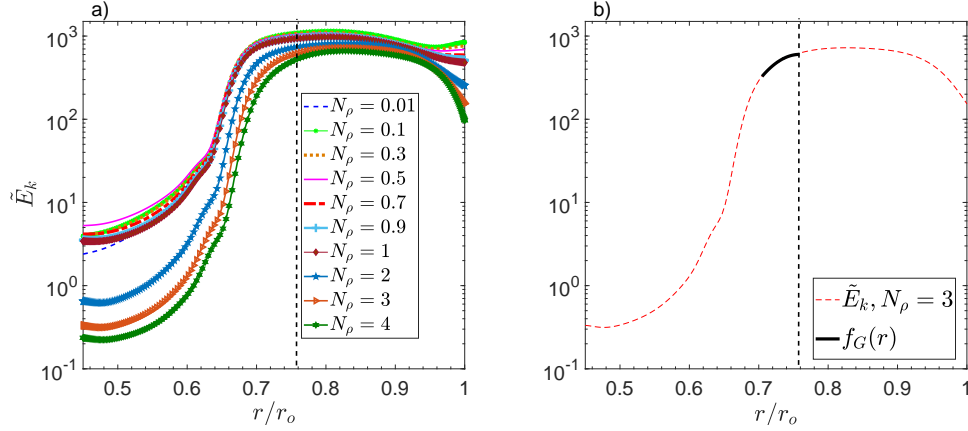


Figure 4. Time- and spherically- averaged kinetic energy profile $\tilde{E}_k(r)$ versus r/r_o at $Ra = 10^5$. The black dashed vertical line corresponds to the base of the convective region. a) The profiles of $\tilde{E}_k(r)$ are shown for all of the different N_ρ cases. $\tilde{E}_k(r)$ decays as a half-Gaussian below the base of the CZ. b) Profile of $\tilde{E}_k(r)$ along with the fitted Gaussian function $f_G(r)$ (see Eq. (19)) below the base of the CZ for the case with $N_\rho = 3$.

convective motions with increased stratification leading to somewhat smaller kinetic energies in the CZ¹. On the other hand, the density ratio in the RZ dictates how strongly stably stratified that region is. We thus conclude that the overshoot lengthscale will depend on the density ratios in both the CZ and the RZ which can be described by R_ρ .

Finally, in Figure 6b, we present a snapshot of the radial velocity for the case of $N_\rho = 3$ and $Ra = 10^5$ at a chosen longitude against r/r_o and θ along with the distance down to $r_c - \delta_G$ marked with a blue solid line to illustrate the computed overshoot distance from the bottom of the CZ (black dashed line). We find that δ_G marks the distance down to which the convective motions overshoot in an average sense.

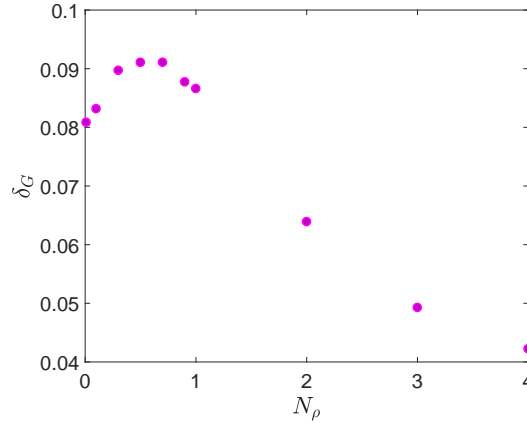


Figure 5. Dependence of the computed overshoot lengthscale δ_G on the density stratification in the CZ N_ρ at $Ra = 10^5$. The lengthscale δ_G increases for $N_\rho \lesssim 0.7$ and decreases for $N_\rho > 0.7$ indicating a non-monotonic dependence on N_ρ .

We now briefly focus on the “penetrative” dynamics associated with thermal mixing in the stable region. To do so, we define the time- and spherically- averaged total adjusted entropy gradient profile $d\tilde{S}_T/dr$ such that

$$\frac{d\tilde{S}_T}{dr} = \frac{d\bar{S}}{dr} + \frac{d\tilde{S}}{dr}, \quad (21)$$

¹ Note that the magnitude of the kinetic energy decreases somewhat with increasing N_ρ due to the fact that all cases shown in Section 3 use $Ra = 10^5$, but with increasing N_ρ , the critical Rayleigh number also increases (see e.g., Jones et al. 2009; Gastine & Wicht 2012), so they do not effectively have the exact same supercriticality.

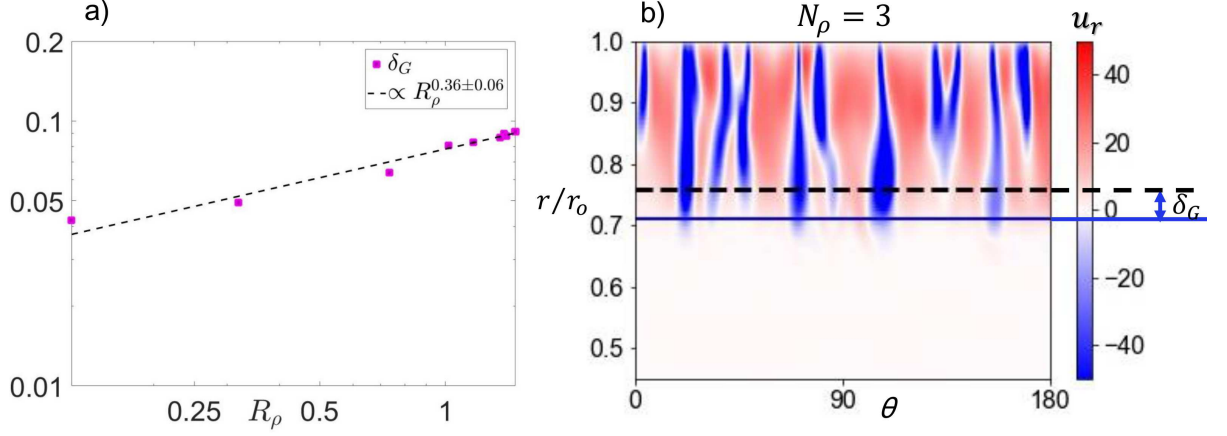


Figure 6. a) Dependence of δ_G on the ratio of the density stratification in the RZ over the one in the CZ given by the parameter R_ρ . The overshoot lengthscale is $\delta_G = 0.078 R_\rho^{0.36}$. b) Snapshot of the radial velocity u_r in r/r_o and θ at a fixed longitude for the $Ra = 10^5$ and $N_\rho = 3$ run. The black dashed line indicates the bottom of the CZ, and the blue solid line indicates the depth down to $r_c - \delta_G$. The overshoot lengthscale δ_G characterizes remarkably well the depth in the RZ down to which the convective motions overshoot on average.

i.e. the sum of the reference entropy gradient and the gradient of the entropy fluctuations. In Figure 7, we plot the background reference $d\bar{S}/dr$ profile and compare it to the adjusted $d\tilde{S}_T/dr$ for four N_ρ cases spanning a wide range of density stratifications. We find that there is some partial thermal mixing in the RZ. Indeed, $d\tilde{S}_T/dr$ deviates somewhat from the background $d\bar{S}/dr$ there and exhibits some slight dependence on N_ρ . However, $d\tilde{S}_T/dr > 0$ in all cases, namely the CZ does not further extend into the stable zone, so no pure penetration is observed. In fact, there appears to be a slightly subadiabatic layer near the base of the convective region. Although this is not a standard feature in 3D overshooting simulations, it has been previously reported in the 3D compressible overshoot simulations of Käpylä et al. (2017) for the cases where they employed a heat conduction profile, based either on a Kramers-like opacity or a static profile of similar shape, which varied smoothly between the CZ and the RZ. Thus, we attribute the subadiabatic layer observed in our runs to our chosen background entropy gradient profile which transitions smoothly from the CZ down to the RZ as well as to the fact that at this Ra , the degree of buoyant driving is not sufficiently strong to establish a fully adiabatic convective interior.

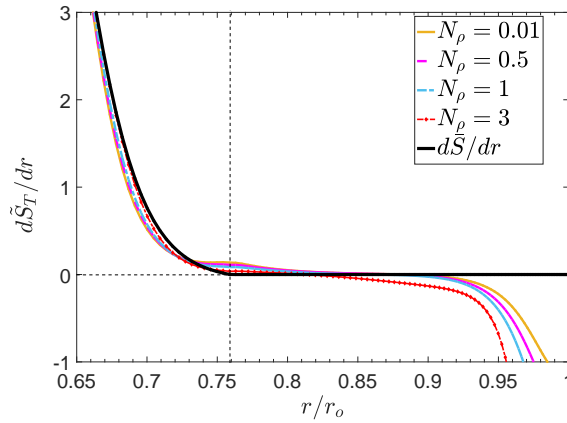


Figure 7. Time- and spherically- averaged total adjusted entropy gradient profile $d\tilde{S}_T/dr$ against r/r_o for four N_ρ cases compared with the background $d\bar{S}/dr$. The black dashed vertical line corresponds to the base of the convective region. The weak partial thermal mixing in the RZ has a slight dependence on N_ρ .

Table 1. Input and output parameters of the simulations

Case	N_ρ	Ra	Ek	Ra_r	Ro_c	$N_r \times N_\theta \times N_\phi$	Ro	δ_G	Re
1	0.01	10^5	$192 \times 528 \times 1056$...	0.081	44.05
2	0.1	10^5	$192 \times 528 \times 1056$...	0.083	43.55
3	0.3	10^5	$192 \times 528 \times 1056$...	0.090	42.44
4	0.5	10^5	$192 \times 528 \times 1056$...	0.091	41.58
5	0.7	10^5	$192 \times 528 \times 1056$...	0.091	40.37
6	0.9	10^5	$192 \times 528 \times 1056$...	0.088	39.48
7	1	10^5	$192 \times 528 \times 1056$...	0.087	39.08
8	2	10^5	$192 \times 528 \times 1056$...	0.064	35.60
8a	2	10^5	0.001	10	0.158	$192 \times 528 \times 1056$	0.0072	0.014	14.33
8b	2	10^5	0.01	215.4	1.58	$192 \times 528 \times 1056$	0.2627	0.045	52.53
8c	2	10^5	0.1	4642	15.8	$192 \times 528 \times 1056$	1.8066	0.061	36.13
9	3	10^4	$192 \times 256 \times 512$...	0.049	13.31
9a	3	10^4	0.01	21.5	0.5	$192 \times 256 \times 512$	0.0423	0.018	8.46
9b	3	10^4	0.1	464.2	5	$192 \times 256 \times 512$	0.6855	0.048	13.71
10	3	10^5	$192 \times 528 \times 1056$...	0.049	33.54
10a	3	10^5	0.001	10	0.158	$192 \times 792 \times 1584$	0.0067	0.013	13.47
10b	3	10^5	0.01	215.4	1.58	$192 \times 528 \times 1056$	0.2263	0.039	45.26
10c	3	10^5	0.1	4642	15.8	$192 \times 528 \times 1056$	1.6991	0.049	33.98
11	3	10^6	$192 \times 1104 \times 2208$...	0.048	81.20
11a	3	10^6	0.001	100	0.5	$192 \times 1104 \times 2208$	0.0432	0.028	86.39
11b	3	10^6	0.01	2154	5	$192 \times 1104 \times 2208$	0.5093	0.047	101.86
12	4	10^5	$192 \times 528 \times 1056$...	0.042	31.87

NOTE—Columns 2 – 6 indicate the input parameters, column 7 provides the resolution and columns 8 – 10 report on the output parameters for both the non-rotating and the rotating simulations.

4. EFFECT OF ROTATION ON THE OVERSHOOTING DYNAMICS

Our work is motivated by solar-type stars, and so we are particularly interested in studying the effect of rotation on the overshooting dynamics. The solar tachocline, for instance, coincides with the region of overshoot near the base of the solar convection zone, and so understanding the effects of rotation within that region represents an important step toward gaining a better understanding of the tachocline dynamics as well. In this Section, we investigate the effect of rotation on the convective overshooting dynamics by considering a series of numerical experiments where we vary N_ρ , Ra and Ek. To categorize each case and the corresponding rotational regime, we output the Rossby number Ro defined as

$$Ro = \frac{U}{2L\Omega_0} = \frac{ReEk}{2}, \quad (22)$$

which is the ratio of inertial forces to the Coriolis force. Here, the first expression includes dimensional quantities where U is a typical dimensional velocity in the CZ, while the second expression includes non-dimensional quantities where $Re = UL/\nu$ is the Reynolds number extracted from the simulations (where $U = u_{rms}\nu/L$). For the value of u_{rms} , we adopt the total (fluctuating part and mean part) velocity averaged over the CZ and weighted by density. Note that the Péclet number Pe is $Pe = PrRe$, so it is simply $Pe = Re$ in our $Pr = 1$ runs.

In Table 1, we also report on the reduced Rayleigh number $Ra_r = RaEk^{4/3}$ which is a typical measure of supercriticality in simulations of rotating convection as well as on the convective Rossby number $Ro_c = \sqrt{RaEk^2/(4Pr)}$ which is a measure of the influence of rotation on the global flows based on the input parameters Ra, Pr and Ek.

We begin by qualitatively examining the flow characteristics for models with four representative values of the resulting Ro. In Fig. 8, we present snapshots of shell slices of the radial velocity u_r close to the outer boundary of the spherical

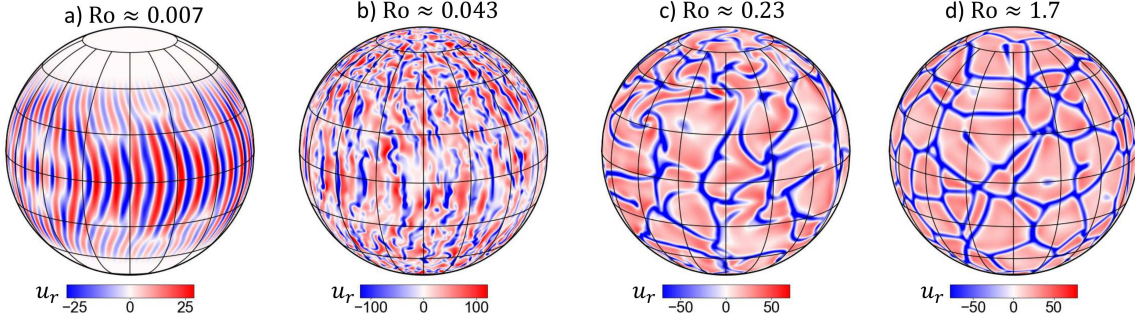


Figure 8. Snapshots of shell slices of the radial velocity u_r at $r = 0.9r_o$, i.e. close to the surface of the spherical shell for a) $Ro \approx 0.007$ at $Ra = 10^5$ and $Ek = 0.001$, b) $Ro \approx 0.043$ at $Ra = 10^6$ and $Ek = 0.001$, c) $Ro \approx 0.23$ at $Ra = 10^5$ and $Ek = 0.01$, and d) $Ro \approx 1.7$ at $Ra = 10^5$ and $Ek = 0.1$. The flow becomes more aligned with the axis of rotation with decreasing values of Ro .

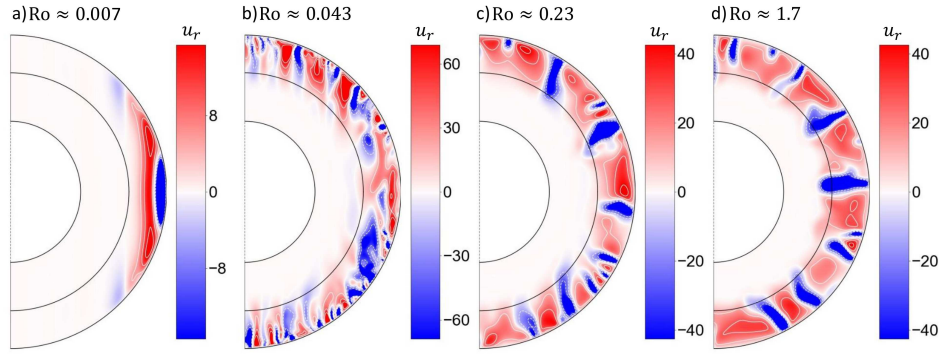


Figure 9. Snapshots of meridional slices of the radial velocity u_r varying in r and θ at a selected longitude for four different values of Ro with a) $Ro \approx 0.007$, $Ra = 10^5$ and $Ek = 0.001$, b) $Ro \approx 0.043$, $Ra = 10^6$ and $Ek = 0.001$, c) $Ro \approx 0.23$, $Ra = 10^5$ and $Ek = 0.01$, and d) $Ro \approx 1.7$, $Ra = 10^5$ and $Ek = 0.1$. The amount of overshooting below the base of the convection zone seems to be decreasing with decreasing Ro .

shell at $r = 0.9r_o$, for cases with Ro spanning values from 0.007 up to 1.7. We notice that for the highest values of Ro , the convective flow is not significantly affected by rotation with the $Ro \approx 0.23$ case exhibiting only a slight alignment of the flow with the axis of rotation within the equatorial region. For the smaller $Ro \approx 0.043$ run, the flow is more columnar near the equator and mid-latitudes while the plumes observed closer to the poles indicate that inertia is dominant there. For the lowest Ro case of $Ro \approx 0.007$, rotation dominates the flow and leads to a purely columnar profile at mid-latitudes and the equator, while u_r is negligible at the poles.

To obtain a qualitative view of the fluid motions across the shell, we show snapshots of meridional slices of u_r versus θ and r at a fixed longitude for the same four computed Rossby numbers in Fig. 9. We observe that for the highest $Ro \approx 1.7$ case, where the Coriolis force is relatively weak, convective motions overshoot a substantial distance below the base of the CZ. As Ro decreases to $Ro \approx 0.23$, the convective motions begin to align with the axis of rotation but still overshoot into the RZ. As Ro decreases further, convective motions increasingly align with the rotation axis, both in the convection zone and in the region of overshoot. Moreover, from a visual inspection, we find that, at least qualitatively, the convective motions seem to overshoot smaller distances into the RZ with decreasing Ro .

We next compute the overshoot lengthscale δ_G for each run, following the same process we used in Section 3. However, for these rotating cases, we fit the Gaussian function (Eq. (19)) to the fluctuating kinetic energy profile $\tilde{E}_f(r)$ (where $\tilde{E}_f(r) = (1/2)\bar{\rho}[u_{f,r}^2 + u_{f,\theta}^2 + u_{f,\phi}^2]$). This definition filters out the mean, axisymmetric flows that arise in rotating convection. Note that $\mathbf{u} = \mathbf{u}_m + \mathbf{u}_f$ where \mathbf{u}_m is the mean, axisymmetric part of the velocity corresponding to the larger-scale motions associated with rotation and \mathbf{u}_f is the fluctuating part of velocity field associated with the convective motions.

In Fig. 10, we present a plot of the values of δ_G along with their errorbars (arising from uncertainty in the fit) against Ro . We note that the errorbars are quite significant in the rotationally-constrained cases of $Ro \ll 0.01$ where

the kinetic energy profiles are not well-fit by the Gaussian below r_c . There, the weak convective motions have already begun to exponentially decay within the bulk of the CZ. Thus, we verify the qualitative behavior illustrated in Fig. 9 and find that δ_G decreases with decreasing Ro as $\delta_G \propto \text{Ro}^{0.23}$.

The fact that δ_G decreases with decreasing Ro is somewhat expected, since the enhanced horizontal interaction associated with rotation can lead to faster braking of the convective overshooting motions within the regimes where the Coriolis force plays a more dominant role. There, the convective flow aligns with the rotation axis, forcing the downflows to overshoot from an angle. Then, the intrinsically radial buoyancy braking in the RZ leads to a more efficient halting of the overshooting motions since it only has to counteract their radial component. This can be viewed qualitatively in Fig. 9, which clearly shows that the radial flow is more aligned with the axis of rotation for lower values of Ro.

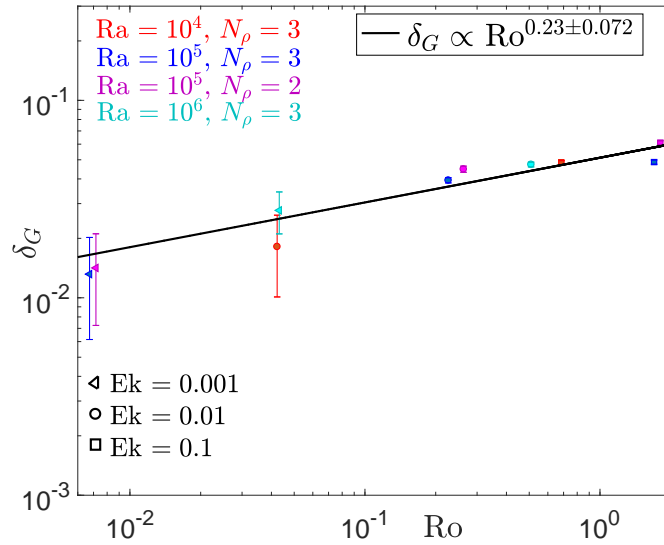


Figure 10. Dependence of the computed overshoot lengthscale δ_G on Rossby number Ro. Error bars associated with uncertainty in the fit are indicated. The black line is the fitted function that describes how δ_G scales with respect to Ro, namely $\delta_G \propto \text{Ro}^{0.23 \pm 0.072}$. The different colors correspond to different Ra and N_ρ indicated in the upper left corner of the plot, while the different shapes correspond to the different values of Ek (shown in the lower left corner of the plot).

More quantitatively, in Figure 11, we illustrate the dependence of the computed overshoot lengthscale δ_G on the latitude θ at the same four representative Ro cases with $\text{Ro} \approx 0.007$, $\text{Ro} \approx 0.043$, $\text{Ro} \approx 0.23$ and $\text{Ro} \approx 1.7$. We find that for $\text{Ro} \approx 1.7$, δ_G only weakly depends on latitude, since the influence of rotation on convection is insignificant. For the $\text{Ro} \approx 0.23$ case, the Coriolis force is somewhat stronger, leading to a shallower δ_G overall which is larger closer to the poles and becomes smaller at mid-latitudes where rotation becomes more dominant. For $\text{Ro} \approx 0.043$, δ_G is considerably larger within the polar regions while it decreases as we approach the mid-latitudes and the equator, commensurate with the fact that the overshooting motions penetrate at an angle there due to the alignment of the convective motions with the axis of rotation (see Fig. 9b). Finally, for the rotationally-constrained case of $\text{Ro} \approx 0.007$, we only show δ_G near the equator, since the extracted δ_G does not give meaningful results away from the equatorial region where the convective motions are much weaker. We see that δ_G in this case is substantially smaller compared with the other Ro cases.

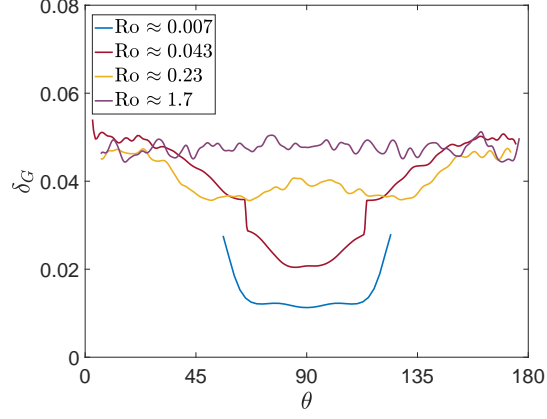


Figure 11. Computed overshoot lengthscale δ_G as a function of latitude θ for four different Ro cases. For larger values of Ro , the latitudinal dependence of δ_G is weaker.

To further examine the dependence of the overshooting dynamics on Ro , in Fig. 12, we plot the time- and spherically-averaged non-dimensional radial fluxes (multiplied by the surface area $4\pi r^2$), namely the kinetic energy flux \tilde{F}_k , the enthalpy flux \tilde{F}_e , the conductive flux \tilde{F}_c , and the viscous flux \tilde{F}_v . These are respectively given by

$$\tilde{F}_k(r) = \frac{\text{DiPr}}{2\text{Ra}} \overline{\rho(u_r \mathbf{u}^2)}, \quad (23)$$

$$\tilde{F}_e(r) = \overline{\rho(u_r T)}, \quad (24)$$

$$\tilde{F}_c(r) = \overline{\rho T} \left(\frac{\partial \tilde{S}}{\partial r} \right), \quad (25)$$

$$\tilde{F}_v(r) = -\frac{\text{DiPr}}{\text{Ra}} \overline{(\mathbf{u} \cdot \mathbf{D})_r}, \quad (26)$$

for the four typical Rossby cases ranging from $Ro \approx 0.007$ to $Ro \approx 1.7$. On the same figure, we also show the radiative flux as given in Eq. (7) as well as the total flux

$$\tilde{F}_{tot} = F_{rad} + \tilde{F}_k + \tilde{F}_e + \tilde{F}_c + \tilde{F}_v. \quad (27)$$

We find that, compared with the lower Ro cases, the runs with $Ro \approx 1.7$ and $Ro \approx 0.23$ attain a substantially larger kinetic energy flux \tilde{F}_k within the CZ and the overshoot region due to the fact that convection is very weakly affected by rotation (as also verified in Fig. 9 and Fig. 10). By contrast, in the lower Rossby case of $Ro \approx 0.043$, \tilde{F}_k is quite small within the CZ while it becomes negligible at $Ro \approx 0.007$ whereby rotation has dominated the dynamics. Similarly, \tilde{F}_e starts decreasing within the CZ but the enthalpy flux is still non-zero below the base of the CZ where the convective motions overshoot. Overall, the magnitude of \tilde{F}_e decreases with decreasing Ro , once again confirming that convection becomes less efficient at larger rotation rates. Finally, \tilde{F}_c increases with decreasing Ro illustrating that heat is mainly transported by conduction once rotation becomes stronger. In all four cases however, \tilde{F}_v is very small, suggesting that viscosity does not play a dominant role in the dynamics.

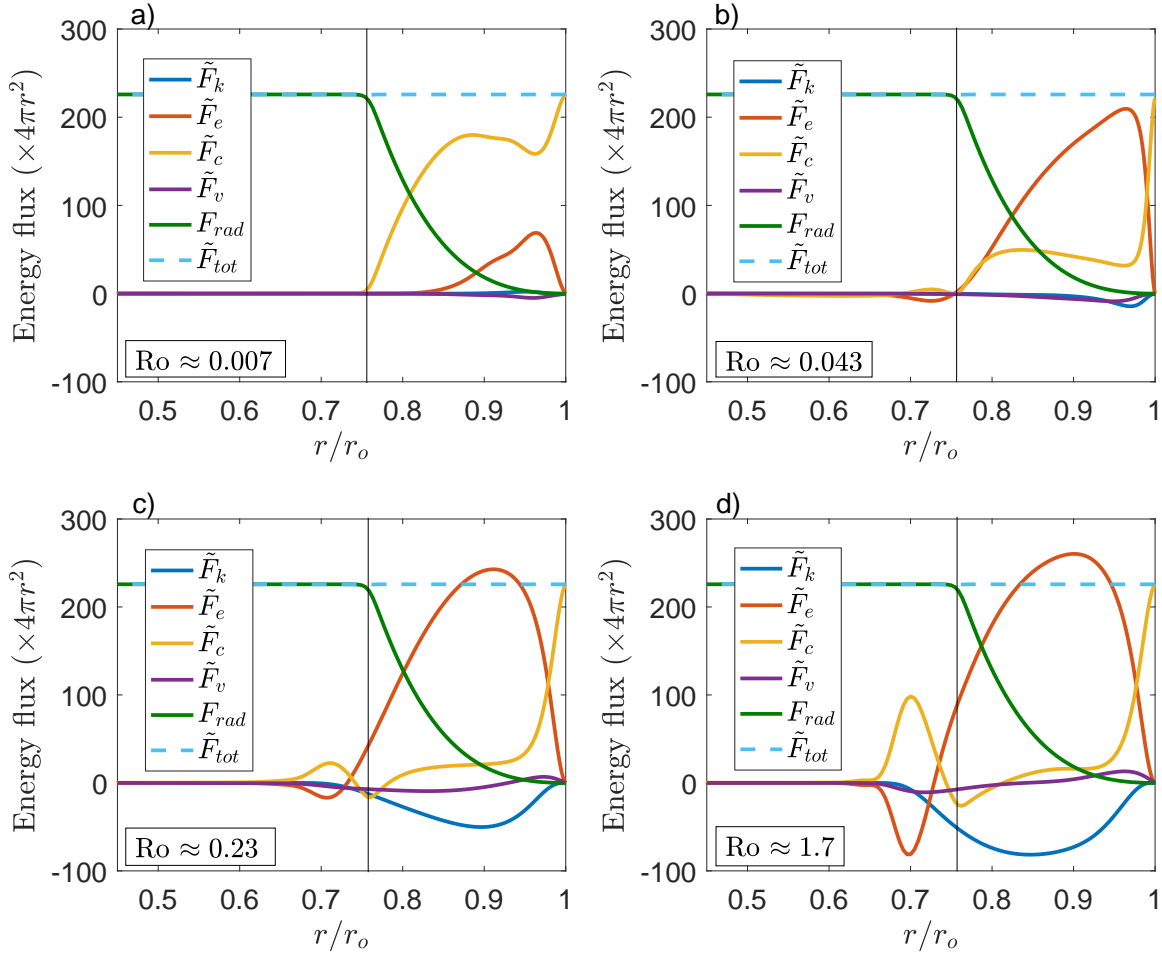


Figure 12. Profiles of the time- and spherically- averaged non-dimensional radial fluxes multiplied by the surface area $4\pi r^2$ against the radius r/r_o with a) $Ro \approx 0.007$ at $Ra = 10^5$ and $Ek = 0.001$, b) $Ro \approx 0.043$ at $Ra = 10^6$ and $Ek = 0.001$, c) $Ro \approx 0.23$ at $Ra = 10^5$ and $Ek = 0.01$, and d) $Ro \approx 1.7$ at $Ra = 10^5$ and $Ek = 0.1$. The black vertical line corresponds to the base of the convective region.

5. MEAN FLOWS AND ANGULAR MOMENTUM BALANCES

5.1. Rotational Profiles and Mean Flows

In Section 4, we focused on the fluctuating component of the kinetic energy in order to understand the dependence of the convective overshooting motions on Ro . We now concentrate on the differential rotational profiles and the associated dynamics within the different regimes arising at different Ro cases. We also investigate the mean flows resulting from velocity correlations due to the presence of rotation through the Coriolis force. In Fig. 13, we present slices of the time- and azimuthally- averaged meridional circulation streamlines with the underlying contours of the mass flux (left panels) and differential rotation profiles ($\langle u_\phi \rangle / (r \sin \theta)$) (right panels) for the four typical Ro cases. We see that for $Ro \approx 0.007$, there are two large cells in the meridional circulation within the CZ and the overshoot region and four smaller ones close to the outer CZ boundary. All of these cells are localized at mid-latitudes and the equator where the flow motions are the strongest (also see Fig. 9a), similarly to the differential rotation. We notice that the equator rotates faster than the poles, but convection in this case is inhibited by rotation, so it is in a rotationally-constrained regime. At $Ro \approx 0.043$, the profile exhibits a multi-cellular flow near the equator that propagates into the RZ particularly within the equatorial region. The differential rotation is again much stronger at the equator and decreases at mid-latitudes and the poles in the CZ while the stable region rotates almost uniformly.

This rotational profile is qualitatively similar to the one observed in the solar CZ, although the latter is conical and not cylindrical as the one in this case. We will refer to this case as the “solar-like” case. At $\text{Ro} \approx 0.23$, the meridional circulation has two distinct large cells within the CZ, while the differential rotation in the CZ is now characterized by faster rotating poles and a slower equator, and is more or less uniform in the bulk of the RZ. Hence, we will refer to this case as “anti-solar” (e.g., [Gastine et al. 2014](#)). Finally, in the largest $\text{Ro} \approx 1.7$ case, the Coriolis force is very weak, and convection is not significantly affected by rotation. The meridional circulation consists of multiple cells and the convection zone now rotates uniformly at a slower rate than the RZ. Overall, in all of these cases (except for the rotationally-constrained case of $\text{Ro} \approx 0.007$), there is significant propagation of the meridional circulation into the stable layer, even beyond the overshoot region.

To understand this behavior more quantitatively, in Fig. 14, we plot the time- and spherically- averaged non-dimensional kinetic energy related to the differential rotation \tilde{E}_{DR} and the meridional circulation \tilde{E}_{MC} as a function of radius where

$$\tilde{E}_{DR}(r) = \frac{1}{2} \bar{\rho} \widetilde{u_{m,\phi}^2}, \quad (28)$$

$$\tilde{E}_{MC}(r) = \frac{1}{2} \bar{\rho} (\widetilde{u_{m,r}^2} + \widetilde{u_{m,\theta}^2}). \quad (29)$$

In Fig. 14a, we see that the kinetic energy associated with the differential rotation $\tilde{E}_{DR}(r)$ is largest for the solar-like case and the anti-solar case both in the CZ and the RZ. It becomes very small at $\text{Ro} \approx 1.7$, where the rotational influence is almost negligible, and in the lowest $\text{Ro} \approx 0.007$ case where the motions are very weak overall and are unable to redistribute angular momentum as efficiently. Moreover, in all four cases, \tilde{E}_{DR} decreases with depth in the CZ, but there is still considerable kinetic energy below the base of the CZ (with the exception of $\text{Ro} \approx 0.007$).

As shown in Fig. 14b, the kinetic energy associated with the meridional flows $\tilde{E}_{MC}(r)$ decreases with decreasing Ro in the CZ and is very small for the lowest $\text{Ro} \approx 0.007$ case (both in the CZ and in the RZ) where rotation dominates the dynamics. For the higher Ro cases, there is substantial kinetic energy in the meridional flows within the overshoot region and part of the stable zone. This indicates that these larger-scale mean flows, although mostly generated in the CZ, do not merely stop at the base of the convective region, but they travel deeper into the radiative zone.

5.2. Angular Momentum Transport

We now focus on the solar-like case and the anti-solar case with $\text{Ro} \approx 0.043$ and $\text{Ro} \approx 0.23$ respectively. We look at the angular momentum transport and the main processes responsible for redistributing angular momentum within the two-zone spherical shell. Following [Elliott et al. \(2000\)](#) and [Brun et al. \(2004\)](#), by taking the ϕ component of the momentum equation, and assuming a statistically stationary state, averaged in time and longitude, we obtain

$$\frac{1}{r^2} \frac{\partial(r^2 \langle F_r(r, \theta) \rangle)}{\partial r} + \frac{1}{r \sin \theta} \frac{\partial(\sin \theta \langle F_\theta(r, \theta) \rangle)}{\partial \theta} = 0. \quad (30)$$

The radial flux $F_r(r, \theta)$ and the latitudinal flux $F_\theta(r, \theta)$ can be expressed non-dimensionally as

$$F_r(r, \theta) = \bar{\rho} r \sin \theta \left(u_{f,r} u_{f,\phi} + u_{m,r} u_{m,\phi} + \frac{u_{m,r} r \sin \theta}{\text{Ek}} + r \frac{\partial}{\partial r} \left(-\frac{u_{m,\phi}}{r} \right) \right), \quad (31)$$

and

$$F_\theta(r, \theta) = \bar{\rho} r \sin \theta \left(u_{f,\theta} u_{f,\phi} + u_{m,\theta} u_{m,\phi} + \frac{u_{m,\theta} r \sin \theta}{\text{Ek}} + \frac{\sin \theta}{r} \frac{\partial}{\partial \theta} \left(-\frac{u_{m,\phi}}{\sin \theta} \right) \right), \quad (32)$$

respectively. We can then consider the time- and azimuthal- average of the individual terms in Eq. (31) such that

$$F_{r,R} = \langle \bar{\rho} r \sin \theta (u_{f,r} u_{f,\phi}) \rangle, \quad (33)$$

$$F_{r,M} = \langle \bar{\rho} r \sin \theta (u_{m,r} u_{m,\phi}) \rangle, \quad (34)$$

$$F_{r,C} = \left\langle \bar{\rho} r \sin \theta \left(\frac{u_{m,r} r \sin \theta}{\text{Ek}} \right) \right\rangle, \quad (35)$$

$$F_{r,V} = \left\langle \bar{\rho} r \sin \theta \left(-r \frac{\partial}{\partial r} \left(\frac{u_{m,\phi}}{r} \right) \right) \right\rangle. \quad (36)$$

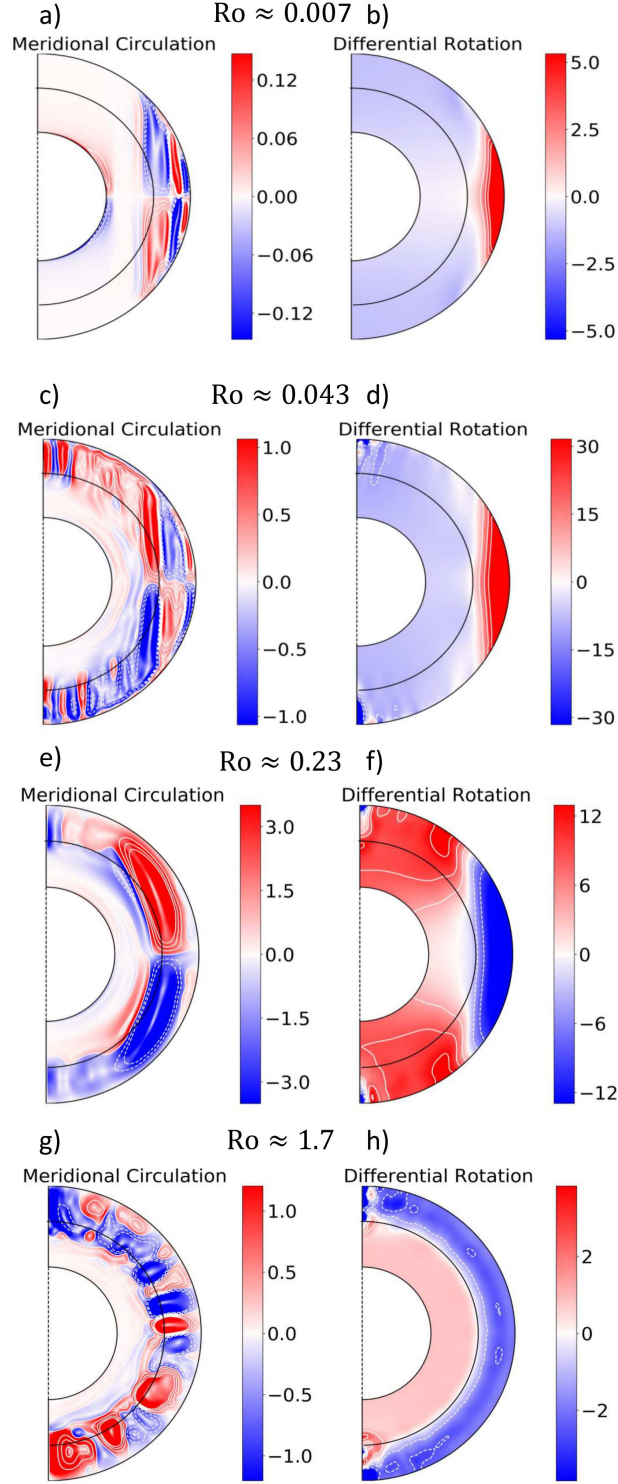


Figure 13. Meridional slices illustrating the meridional circulation streamlines with underlying contours of the mass flux $\pm\sqrt{\langle \bar{\rho} u_r^2 \rangle + \langle \bar{\rho} u_\theta^2 \rangle}$ (blue color corresponds to clockwise motion, and red color to counter-clockwise) and the differential rotation profiles $\langle u_\phi \rangle / (r \sin \theta)$, respectively for a), b) $Ro \approx 0.007$ at $Ra = 10^5$ and $Ek = 0.001$, c), d) $Ro \approx 0.043$ at $Ra = 10^6$ and $Ek = 0.001$, e), f) $Ro \approx 0.23$ at $Ra = 10^5$ and $Ek = 0.01$, and g), h) $Ro \approx 1.7$ at $Ra = 10^5$ and $Ek = 0.1$.

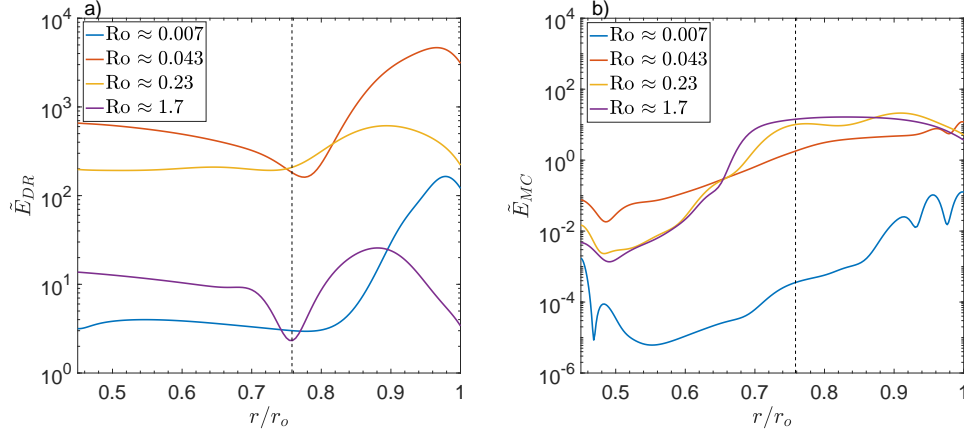


Figure 14. Time- and spherically- averaged non-dimensional kinetic energy in the mean flows. The black dashed vertical line corresponds to the base of the convective region. a) Profile of the kinetic energy related to the differential rotation $\tilde{E}_{DR}(r)$. $\tilde{E}_{DR}(r)$ is largest for the solar-like and the anti-solar cases in the CZ and the RZ. b) Profile of the kinetic energy associated with the meridional circulation $\tilde{E}_{MC}(r)$ for four different values of Ro . For the three highest Ro cases, $\tilde{E}_{MC}(r)$ is substantially large below the base of the CZ indicating that the mean flows propagate into the RZ.

In a similar manner, the individual terms in Eq. (32) are

$$F_{\theta,R} = \langle \bar{\rho} r \sin \theta (u_{f,\theta} u_{f,\phi}) \rangle, \quad (37)$$

$$F_{\theta,M} = \langle \bar{\rho} r \sin \theta (u_{m,\theta} u_{m,\phi}) \rangle, \quad (38)$$

$$F_{\theta,C} = \left\langle \bar{\rho} r \sin \theta \left(\frac{u_{m,\theta} r \sin \theta}{Ek} \right) \right\rangle, \quad (39)$$

$$F_{\theta,V} = \left\langle \bar{\rho} r \sin \theta \left(-\frac{\sin \theta}{r} \frac{\partial}{\partial \theta} \left(\frac{u_{m,\phi}}{\sin \theta} \right) \right) \right\rangle. \quad (40)$$

Note that Equations (33) and (37) are associated with the Reynolds stresses, Equations (34) and (38) and Equations (35) and (39) correspond to the mean flows associated with the meridional circulation and finally Equations (36) and (40) are related to the viscous stresses.

In Fig. 15a,b, c and d we show the profiles of the latitudinal fluxes at $Ro \approx 0.043$ (solar-like case). We observe that $F_{\theta,C}$ is large near the equator and at mid-latitudes within the CZ. There is substantial penetration in the stable region where the distinct cells have opposite signs commensurate with the meridional circulation profile in Fig. 13c. Angular momentum in the convection zone and in the overshoot region seems to be dictated by the flux related to the action of the Coriolis force on the mean meridional flows while all the other fluxes are comparatively very small. In Fig. 15e,f,g and h, we notice that the radial flux $F_{r,C}$ is again large within the CZ while it also extends further down into the RZ transporting angular momentum mainly inward. The profile of $F_{r,R}$ shows that transport by Reynolds stresses is weak compared to the transport by $F_{r,C}$, however it does contribute to the overall angular momentum transport with inward transport at mid-latitudes and outward transport near the equator. The flux associated with the mean flows $F_{r,M}$ is negligible, similarly to $F_{\theta,M}$, while $F_{r,V}$ is also small overall although it does seem to become stronger close to the equator within the CZ where it transports angular momentum inward.

For the anti-solar case of $Ro \approx 0.23$, in Figure 16c, we see that, similarly to the solar-like case, $F_{\theta,C}$ is dominant within the CZ and the overshoot region, while $F_{\theta,R}$, $F_{\theta,M}$ and $F_{\theta,V}$ are all much weaker (Fig. 16a,b and d). In Figure 16e,f,g and h, we notice that $F_{r,C}$ is again the largest in magnitude compared with the other fluxes carrying angular momentum outward near the equator and inward at mid-latitudes while $F_{r,R}$ although not as large, is nonetheless present within the CZ carrying angular momentum inward (except at the poles where it is too weak), similarly to the much weaker $F_{r,M}$. Finally, $F_{r,V}$ is mostly larger close to the base of the CZ within the equatorial region transporting angular momentum in the same direction as $F_{r,C}$.

5.3. Thermal-wind Balance within the CZ and the Overshoot Region

We are interested in understanding what balances are achieved and how the mean flows are sustained in a steady state across the two-zone spherical shell. Two dominant terms that contribute to the meridional flows are the rotational

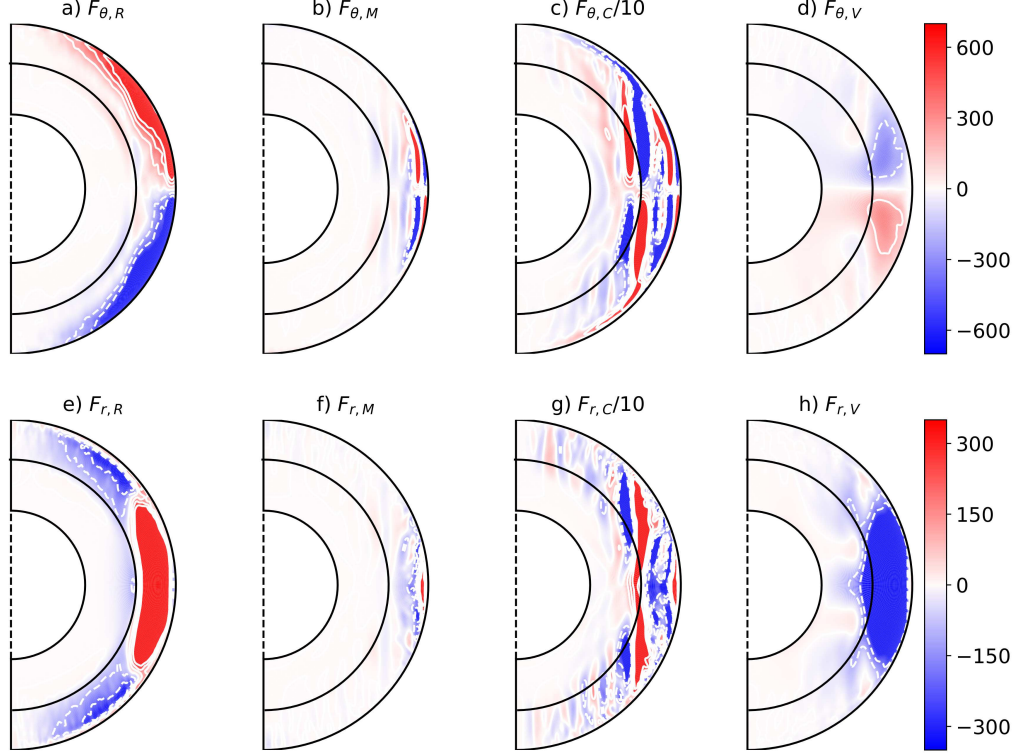


Figure 15. Time- and azimuthally- averaged latitudinal and radial fluxes contributing to the angular momentum transport for the solar-like case with $\text{Ro} \approx 0.043$. The fluxes associated with the Reynolds stresses are shown in panels a) and e), the ones related to the mean flows are shown in b) and f), the ones related to the Coriolis term are shown in c) and g) and the ones associated with the viscous stresses are shown in panels d) and h). The fluxes corresponding to the action of the Coriolis force on the mean flows are dominant and as such we have divided them by 10 (panel c) and g)) in order to highlight the profiles of the other weaker fluxes and examine all of them under the same colorbar.

shear associated with the differential rotation and the baroclinicity of the mean stratification. This balance, known as thermal-wind balance, occurs when the system is in both hydrostatic and geostrophic equilibrium, namely when there is a balance between the Coriolis force, the pressure and the gravity (see e.g., Ruediger 1989; Kitchatinov & Ruediger 1995; Rempel 2005; Miesch et al. 2006; Miesch & Hindman 2011; Acevedo-Arreguin et al. 2013). Within the anelastic approximation, the dimensional thermal-wind equation is then given by

$$\frac{\partial \Omega^2}{\partial z} \approx \frac{g}{\lambda r c_p} \frac{\partial \langle S \rangle}{\partial \theta}, \quad (41)$$

where $z = r \cos \theta$, $\lambda = r \sin \theta$ and $\Omega = \Omega_o + \langle u_\phi \rangle / \lambda$ is the total angular velocity. Non-dimensionally, Eq. (41) can be expressed as

$$\underbrace{\frac{2}{\text{Ek}} \left(r \cos \theta \frac{\partial \langle u_\phi \rangle}{\partial r} - \sin \theta \frac{\partial \langle u_\phi \rangle}{\partial \theta} \right)}_{\text{LHS}} \approx \underbrace{\frac{\text{Ra} g(r)}{\text{Pr}} \frac{\partial \langle S \rangle}{\partial \theta}}_{\text{RHS}}, \quad (42)$$

(where again $\langle \cdot \rangle$ denotes a time- and azimuthally- averaged quantity). In Fig. 17, we examine the thermal-wind balance for the solar-like case with $\text{Ro} \approx 0.043$ and the anti-solar case with $\text{Ro} \approx 0.23$. In Fig. 17a, we plot the left-hand side term (LHS) term and right-hand-side (RHS) term of Eq. (42) at different radii from the bottom of the CZ r_c down to $\sim r_c - \delta_G$ for the solar-like case. The LHS term is associated with the Coriolis force and thus refers to the inertia of the differential rotation, while the RHS term accounts for the baroclinicity of the stratification through the latitudinal gradient of the entropy perturbations. The thermal-wind balance is satisfied within the overshoot region for this solar-like case where $\text{LHS} \approx \text{RHS}$ in that region. In Figure 17b, we also show contours of the LHS and RHS terms with respect to θ and r . We observe that overall, the thermal-wind balance seems to be satisfied across the whole shell, and this is more pronounced within the equatorial region.

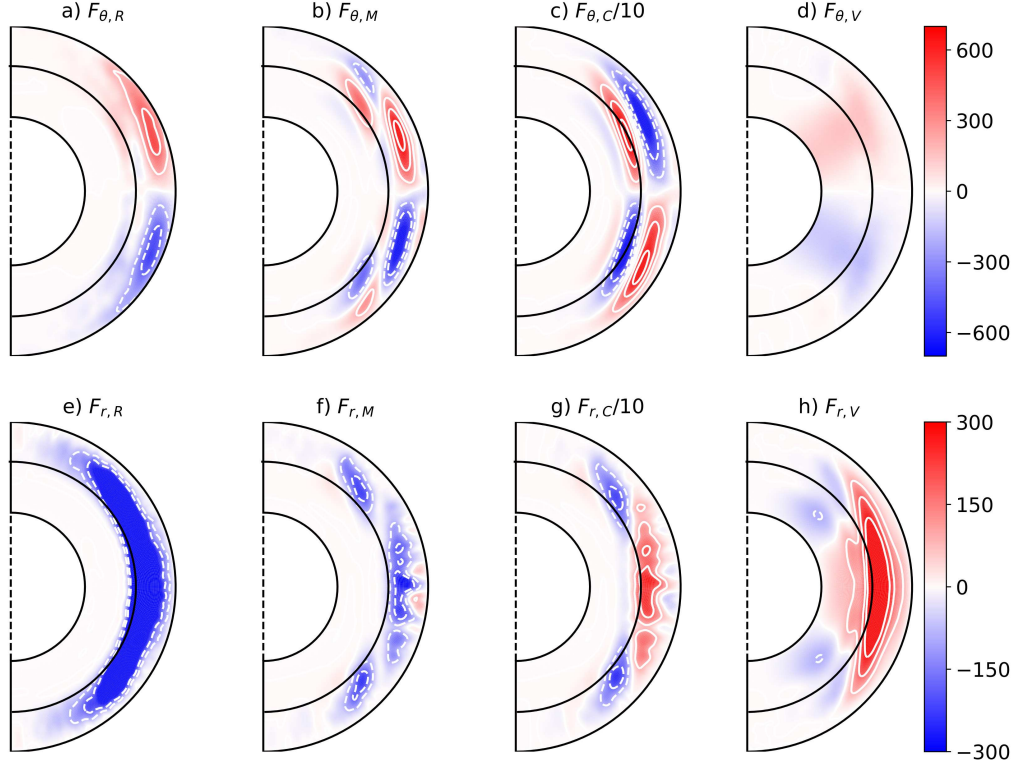


Figure 16. Time- and azimuthally- averaged latitudinal and radial fluxes contributing to the angular momentum transport for the anti-solar case with $\text{Ro} \approx 0.23$. The fluxes associated with the Reynolds stresses are shown in panels a) and e), the ones related to the mean flows are shown in b) and f), the ones related to the Coriolis term are shown in c) and g) and the ones associated with the viscous stresses are shown in panels d) and h). The fluxes corresponding to the action of the Coriolis force on the mean flows are dominant and as such we have divided them by 10 (panel c) and g)) in order to highlight the profiles of the other weaker fluxes and examine all of them under the same colorbar.

Similarly, in Fig. 17c, we plot the LHS and RHS terms of Eq. (42) at all radii from the bottom of the CZ down to $\sim r_c - \delta_G$ for the anti-solar case with $\text{Ro} \approx 0.23$, and we see that the LHS term is somewhat larger than the RHS term within the overshoot region, especially at mid-latitudes. Looking at Fig. 17d, we find that the LHS term is substantially different from the RHS term especially within the convection zone, thus indicating that the thermal-wind balance is not satisfied for the anti-solar case in the CZ, although it is somewhat sustained in the bulk of the stable region. We note that Equation (42) essentially shows that it is possible to maintain non-cylindrical rotational profiles (i.e. when $\text{LHS} \neq 0$) by accounting for latitudinal gradients of $\langle S \rangle$, but we observe no such behavior in this study.

5.4. Gyroscopic Pumping

A well-known mechanism for the generation of meridional circulation via balances in the angular momentum equation, which had been originally extensively studied in the context of the Earth's atmospheric circulation and has been more recently revisited in studies of astrophysical fluid dynamics (McIntyre 2007; Garaud & Acevedo Arreguin 2009; Garaud & Bodenheimer 2010; Wood et al. 2011; Miesch & Hindman 2011), is the so-called gyroscopic pumping. More specifically, gyroscopic pumping is associated with the advection of angular momentum by meridional flow due to the divergence of Reynolds stresses and viscous stresses. We now briefly explore the gyroscopic pumping balances in the solar-like case and the anti-solar case to see whether this mechanism takes place in both of these representative runs as well as which fluxes are dominant in maintaining it in the convective zone and the overshoot region.

Taking the zonal component ϕ of the momentum equation and multiplying it by $\lambda = r \sin \theta$, averaging over both time and longitude and finally assuming a steady state, we obtain the conservation of angular momentum equation of our system given by

$$\bar{\rho} \langle \mathbf{u}_{mc} \rangle \cdot \nabla \mathcal{L} = -(\nabla \cdot \mathbf{F}_{RS} + \nabla \cdot \mathbf{F}_{VS}) \quad (43)$$

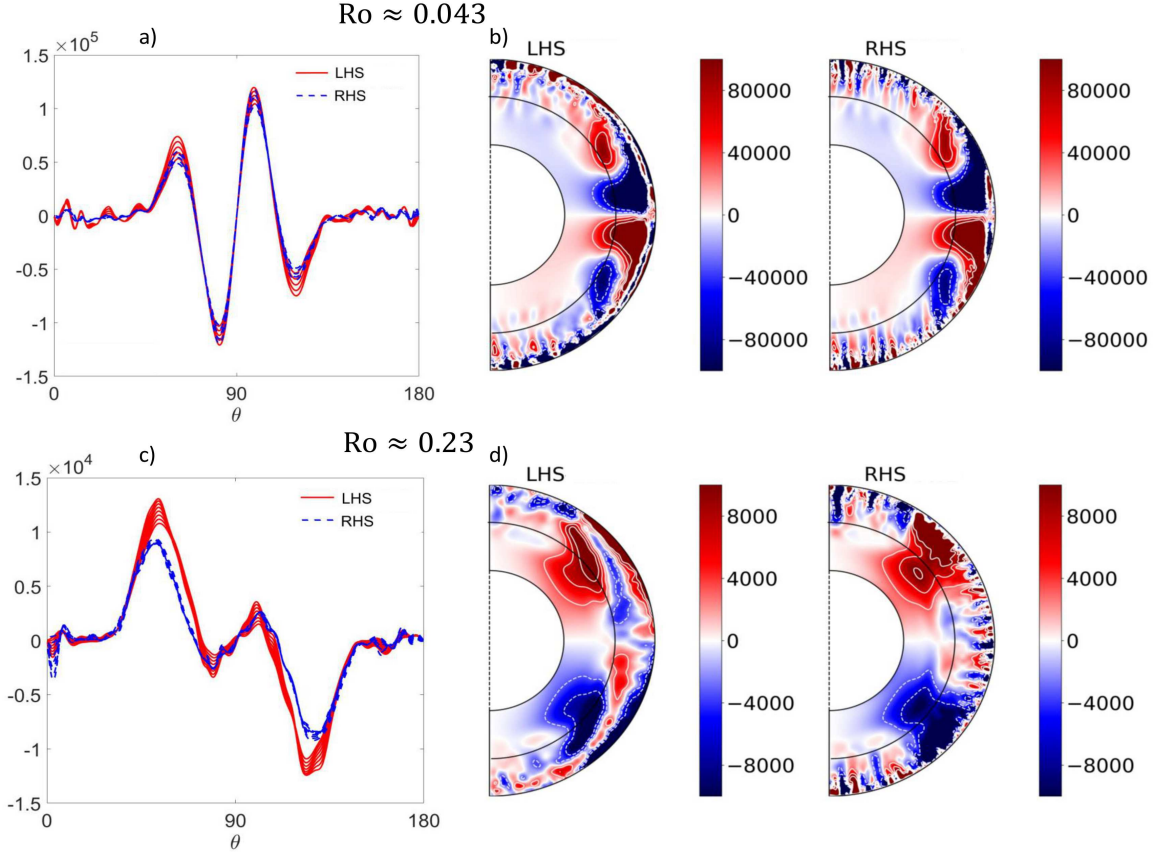


Figure 17. Thermal-wind balance for the solar-like and the anti-solar cases. a) Profile of the LHS part and the RHS part of Equation (42) versus latitude θ at different radii within the overshoot region for the solar-like case with $Ro \approx 0.043$ (similarly for panel c) but for the anti-solar case with $Ro \approx 0.23$). b) Meridional slices of the LHS and RHS terms illustrating the thermal-wind balance across the whole shell for the solar-like case (similarly for panel d) but for the anti-solar case). The thermal-wind balance is mostly satisfied across the shell for the solar-like case but is somewhat sustained only in the RZ for the anti-solar case.

where $\mathbf{u}_{mc} = (u_r, u_\theta)$ and where $\mathcal{L} = \lambda^2 \Omega$, which can be non-dimensionally expressed as

$$\mathcal{L} = r \sin \theta \left(\frac{r \sin \theta}{Ek} + \langle u_\phi \rangle \right). \quad (44)$$

The non-dimensional transport of angular momentum due to Reynolds stresses and due to viscous stresses is given respectively by

$$\mathbf{F}_{RS} = \bar{\rho} r \sin \theta (\langle u_{f,r} u_{f,\phi} \rangle, \langle u_{f,\theta} u_{f,\phi} \rangle), \quad (45)$$

$$\mathbf{F}_{VS} = \bar{\rho} \left(\langle u_{m,\phi} \rangle \sin \theta - r \sin \theta \frac{\partial \langle u_{m,\phi} \rangle}{\partial r}, \langle u_{m,\phi} \rangle \cos \theta - \sin \theta \frac{\partial \langle u_{m,\phi} \rangle}{\partial \theta} \right). \quad (46)$$

Following Featherstone & Miesch (2015), in Figure 18a, we plot the left-hand-side term of Equation (43), i.e. $\bar{\rho} \langle \mathbf{u}_{mc} \rangle \cdot \nabla \mathcal{L}$ along with the right-hand-side term $-(\nabla \cdot \mathbf{F}_{RS} + \nabla \cdot \mathbf{F}_{VS})$ at all radii from r_c down to $\sim r_c - \delta_G$ for the solar-like case with $Ro \approx 0.043$ and find that the balance is more or less achieved within the overshoot region with $\bar{\rho} \langle \mathbf{u}_{mc} \rangle \cdot \nabla \mathcal{L}$ being slightly larger than $-(\nabla \cdot \mathbf{F}_{RS} + \nabla \cdot \mathbf{F}_{VS})$. In fact, by looking across the whole shell in Figure 18b, we find that, overall, Equation (43) is satisfied within the CZ and the overshoot region where the differential rotation and the associated meridional flows are generated and advected. We note that we should not expect Eq. (43) to be satisfied in the bulk of the radiative zone where the motions are not convectively driven and so are largely axisymmetric. Furthermore, we notice that $-\nabla \cdot \mathbf{F}_{RS}$ seems to be dominant in the bulk of the CZ while $-\nabla \cdot \mathbf{F}_{VS}$ is larger at lower latitudes and the equatorial region, especially close and somewhat below the bottom of the CZ.

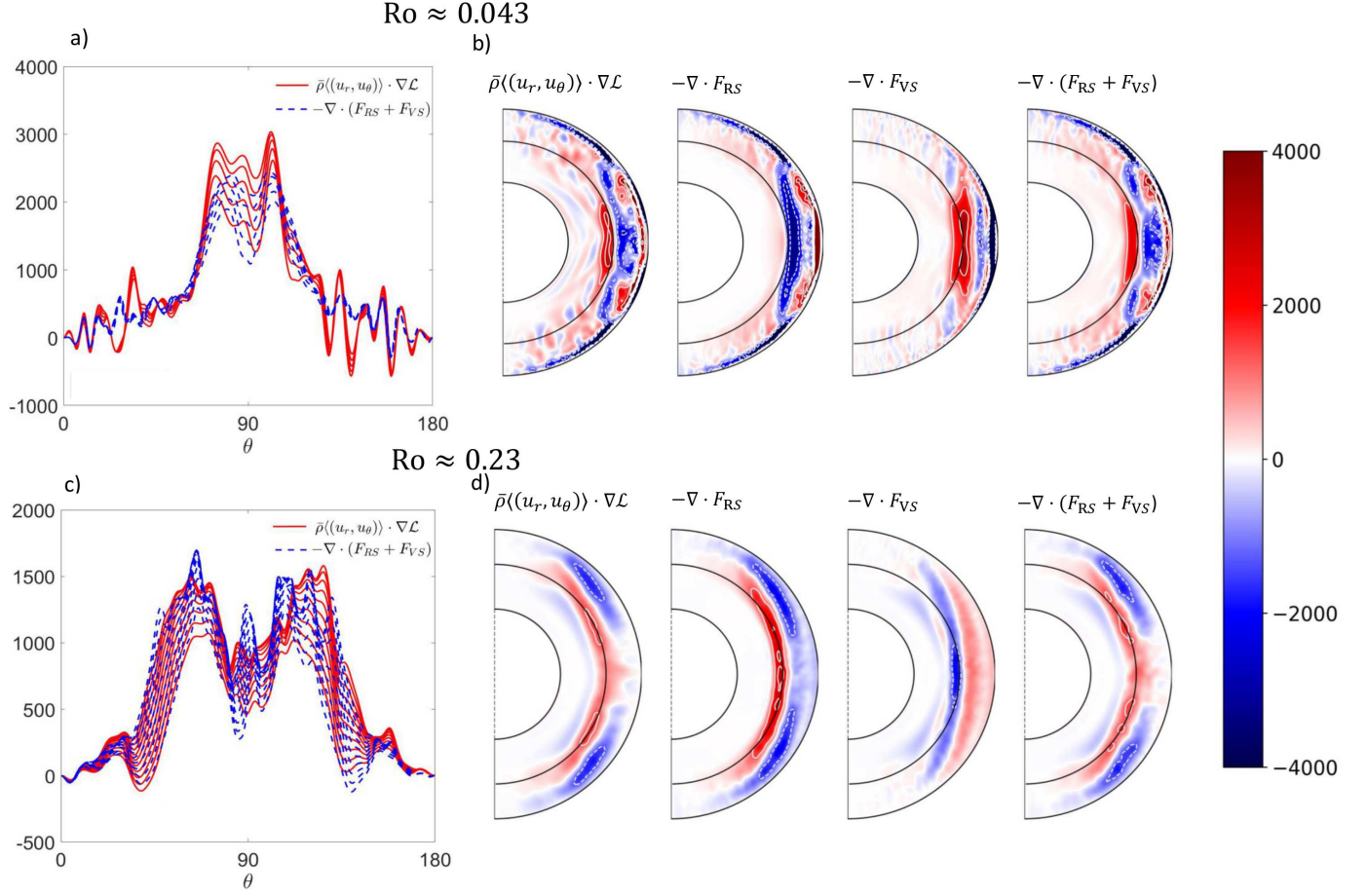


Figure 18. Gyroscopic pumping balances for the solar-like and the anti-solar cases. Profile of the LHS and RHS terms of Equation (43) versus latitude θ at different radii within the overshoot region for the solar-like case with $Ro \approx 0.043$ (similarly for panel c) but for the anti-solar case with $Ro \approx 0.23$). b) Meridional slices of the LHS and RHS terms illustrating the gyroscopic pumping balance across the whole shell for the solar-like case (similarly for panel d) but for the anti-solar case). The gyroscopic pumping balance is overall achieved within the CZ and the overshoot region for both the solar-like case and the anti-solar case.

In Fig. 18c, we show the left-hand-side and the right-hand-side terms of Eq. (43) at different radii within the overshoot region for the anti-solar case with $Ro \approx 0.23$. We observe that the gyroscopic pumping balance seems to be satisfied within that region although there are some discrepancies between the two terms mostly close to the equator with $-(\nabla \cdot \mathbf{F}_{RS} + \nabla \cdot \mathbf{F}_{VS})$ being somewhat larger than $\bar{\rho}\langle\mathbf{u}_{mc}\rangle \cdot \nabla \mathcal{L}$. In Fig. 18d, we plot the individual terms across the whole shell and find that the gyroscopic balance is achieved. Similarly to the solar-like case, the divergence of the flux associated with the Reynolds stresses is dominant throughout the shell while the viscous stresses play a less important role overall and are larger mainly at mid-latitudes and the equatorial region of the CZ.

Stars operate in a regime where viscosity is very small (with typical Prandtl numbers $Pr \sim O(10^{-6})$), so we would expect that the advection of the meridional flows would be due to only the divergence of the fluxes associated with the Reynolds stresses while viscous stresses should be negligible, unlike what we see in the runs presented here. Indeed, viscosity seems to have a fairly strong presence near the equatorial region for both the solar-like case and the anti-solar case which would mean that we may need to consider even higher Ra runs (which are computationally much harder to achieve) so that the viscous stresses would not need to compensate for the weaker Reynolds stresses observed at this Ro and Ra .

6. DISCUSSION

6.1. *Summary of our Results and Comparison with Previous Studies of Overshooting Convection*

We have presented the results of a series of numerical simulations in a two-zone spherical shell in order to examine the effect of rotation and density stratification on the overshooting dynamics associated with the interaction of a convectively unstable region overlying a stably stratified zone. Motivated by solar-type stars, we have assumed a fixed thermal gradient boundary condition at the inner boundary, as well as the existence of an internal heat source whose function mimics the radiative heating presented in more complicated solar models (Model S), while we have used a fixed aspect ratio which corresponds to the inner part of the solar convective region and a large portion of the radiative zone. We have conducted a systematic study by varying the density stratification in the CZ, the Rayleigh number, and the Ekman number while we have assumed a fixed Prandtl number ($\text{Pr} = 1$). To create our two-layered configuration, we have considered a varying background entropy gradient $d\tilde{S}/dr$ which leads to an adiabatic CZ that smoothly transitions into a subadiabatic RZ with a profile fixed for all of our runs – both non-rotating and rotating.

There have been many numerical studies of overshooting convection considering a convective region overlying a stably stratified zone which, as we discussed in Section 1, have been mainly focused on the dependence of the overshooting on the relative stability and the transition width between the two layers as well as the degree of the convective driving in the CZ. In all of these studies, similarly to ours, they found that there is a substantial amount of overshooting δ below the base of the convective region which depends on the input parameters, the different set-ups and geometries, or whether they are 2D or 3D (see e.g., Hurlburt et al. 1986, 1994; Singh et al. 1998; Brummell et al. 2002; Rogers & Glatzmaier 2005; Pratt et al. 2017; Hotta 2017; Käpylä 2019; Korre et al. 2019). For instance, Hurlburt et al. (1986) reported a value of $\delta = 0.67H_p$, Singh et al. (1998) found that δ ranges between $0.4H_p - 0.88H_p$ while Brummell et al. (2002) reported values of δ between $0.4H_p$ and $2H_p$, where H_p is the pressure scale-height. In our runs the pressure scale-height at the bottom of the CZ defined as $H_p = -((1/P(r))dP(r)/dr)^{-1}|_{r=r_c}$ depends on N_ρ and ranges between ~ 0.32 and ~ 46 such that the overshoot lengthscale in terms of pressure scale-heights is $0.0074H_p \leq \delta = \delta_G r_o \leq 0.64H_p$. So our findings are similar to those reported in previous studies, especially when we consider higher N_ρ cases.

We also found that the computed overshoot lengthscale δ_G for the non-rotating cases, which have fixed Pr and Ra , depends on the ratio of the density stratifications in the two zones given by the parameter R_ρ such that $\delta_G \propto R_\rho^{0.36}$. However, to the authors' knowledge, there is no previous systematic study on the dependence of overshooting on the density stratification as an input parameter. A notable exception is the work of Massaguer et al. (1984), who employed the anelastic approximation in a Cartesian geometry and reported the penetration lengthscale for two different density stratification cases while they also compared these results to a Boussinesq case. In their work, they assumed stacked polytropes with a varying conductivity profile such that a convection zone is sandwiched between two stable layers and studied upward and downward penetration. However, they did not perform fully non-linear 3D calculations, but instead they used anelastic modal equations whereby they expanded the horizontal structure of the flow using one- and two-mode hexagonal planforms in order to better resolve the vertical structure. As a result, their findings have a strong dependence on the chosen horizontal modes and cannot capture the fully non-linear dynamics associated with overshooting convection. Nonetheless, they found that the increased density stratification leads to larger penetration and that the anelastic case predicts larger penetration depths than the Boussinesq case. In fact, they reported strong pure penetration whereby the convection zone extended further down into the stable region and part of the latter became adiabatic.

In our work, we do not observe pure penetration but rather overshooting, although there is a trend in the $d\tilde{S}_T/dr$ profiles (see Eq. (21)) indicating that increasing the stratification along with the Rayleigh number even further might actually result in pure penetration. This can be seen in Fig. 19, where we plot the total adjusted $d\tilde{S}_T/dr$ profile along with $d\tilde{S}/dr$ for the case with $N_\rho = 3$ at three different Ra . We also notice that the slightly subadiabatic layer around the base of the CZ (discussed in Section 3) becomes even smaller at larger Ra , where convection is more vigorous.

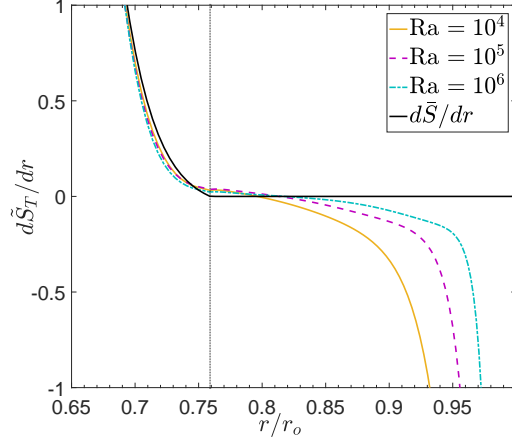


Figure 19. Time- and spherically- averaged total adjusted entropy gradient profile $d\tilde{S}_T/dr$ against r/r_o at $N_\rho = 3$ for three different Rayleigh numbers compared with the background $d\tilde{S}/dr$. The black vertical line corresponds to the base of the convective region. Larger values of Ra lead to stronger partial thermal mixing in the RZ and a smaller subadiabatic layer close to the bottom of the CZ.

Massaguer et al. (1984) also showed that the local Pe decreased with decreasing stratification which is not the case in our fully non-linear 3D calculations where increased density stratification leads to smaller Reynolds (and Péclet numbers) due to somewhat weaker convection at the same Ra for larger N_ρ (see e.g., Jones et al. 2009).

We postulate that in a set-up where N_ρ in the CZ increases but somehow the density ratio in the RZ remains the same for all of the cases, then R_ρ will be a monotonic function of N_ρ and as such it can lead to larger overshoot depths for larger values of N_ρ , but that remains to be verified by simulations which account for such a two-layered configuration.

There have been quite a few previous studies that have accounted for rotation in overshooting convective experiments. Using 3D compressible simulations, Brummell et al. (2002) showed that the overshoot depth decreases with decreasing Ro as a result of the braking of the vertical flows due to the horizontal interactions of the like-sign vortices as well as the fact that the downflows penetrate at an angle in the presence of strong rotation. They reported a scaling of $\delta \propto Ro^{0.15}$ while they also showed that it depends on the latitude with the poles and the equator having larger δ . However, their scaling was a result of only three different cases while they also used the f -plane approximation in a Cartesian box which intrinsically cannot account for global flows. Similarly, Pal et al. (2007) found that δ decreases with Ro with $\delta \propto Ro^{0.2}$ at the poles and $\delta \propto Ro^{0.4}$ at mid-latitudes. Augustson & Mathis (2019) studied overshooting convection under the effect of rotation by building on the linearized model of Zahn (1991) and they reported that the overshoot depth decreases like $Ro^{0.3}$.

In this work, we found that $\delta_G \propto Ro^{0.23}$ which is not that different from the predictions of these previous models, even though we operate in a spherical geometry, using a different set-up based on the anelastic approximation. Thus, the decrease in the amount of overshooting with increasing rotation rate seems to be a salient feature of the rotating overshooting dynamics. Additionally, we showed that the overshoot depth depends on latitude with the solar-like case ($Ro \approx 0.043$) leading to larger overshoot depths closer to the poles and at mid-latitudes where the flow is more weakly influenced by rotation and smaller depths near the equator where the convective motions penetrate at an angle due to their alignment with the axis of rotation. For the anti-solar case ($Ro \approx 0.23$), again the overshoot depth is larger at higher-latitudes while it is just a bit larger close to the equator where the motions are not as much aligned with the axis of rotation as at mid-latitudes. Possibly this is also a result of the topology of the plumes there which appear to be more like the fly-wheeling motions described in Brummell et al. (2002). Overall when increasing Ro the latitudinal dependence becomes weaker due to the smaller effect of the rotation on convection.

We note that other studies of anelastic overshooting convection in spherical shells (see Browning et al. 2004; Brun et al. 2011; Augustson et al. 2012; Brun et al. 2017) showed that the overshoot lengthscale decreases with increasing Rossby number. However, these simulations were not focused on the dependence of the overshooting dynamics on Ro , the measure of the overshoot depth was based on the radial enthalpy flux rather than the full kinetic energy and they were operating at lower Pe . Thus, it is not clear how to draw meaningful comparisons with the results of our study.

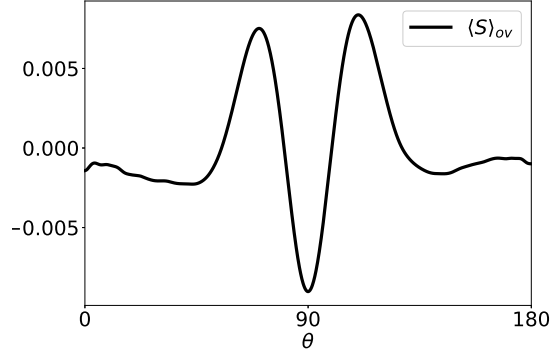


Figure 20. Latitudinal dependence of the time- and azimuthally- averaged entropy perturbations (with their spherically symmetric mean subtracted) volume-averaged within the overshoot region $\langle S \rangle_{ov}$ for the solar-like case with $Ro \approx 0.043$. $\langle S \rangle_{ov}$ does not vary substantially with latitude and exhibits a non-monotonic profile.

6.2. Implications for Overshooting in the Sun

We showed that for sufficiently small Ro , we can obtain a solar-like differential rotation with a faster equator and slower poles in the CZ transitioning to a uniform rotation in the RZ. However, helioseismology has revealed that the Sun also possesses a conical profile while our solutions lead to cylindrical ones.

Previous studies (e.g., [Rempel 2005](#); [Miesch et al. 2006](#)) have shown that enforcing a strong latitudinal entropy gradient at the base of the CZ can result in a conical differential rotation similarly to what we observe in the Sun. Looking at the entropy profile in Fig. 3b of [Miesch et al. \(2006\)](#) (also see Fig.8d from [Matilsky et al. \(2020\)](#) who accounted for a fixed flux outer boundary condition instead of a latitudinal entropy gradient at the inner boundary), we notice that in the solar-like conical profiles achieved in their calculations, the entropy perturbations increase monotonically with latitude away from the equator.

In Figure 20, we show the time- and azimuthally- averaged entropy perturbations (where we have subtracted the spherically symmetric mean to enhance the latitudinal variations), volume-averaged within the overshoot region $\langle S \rangle_{ov}$ versus the latitude θ for the solar-like case of $Ro \approx 0.043$. We observe that $\langle S \rangle_{ov}$ is much weaker in magnitude and does not vary substantially in latitude compared with the entropy profiles corresponding to the conical differential rotation contours in [Miesch et al. \(2006\)](#). Also, despite the fact that the equatorial region is still cooler than the mid-latitudes and the poles, the profile is non-monotonic. These previous studies only considered a convection zone and thus they had to enforce a latitudinal entropy gradient at the inner boundary (or assume a fixed flux outer boundary condition) to achieve the tilt of the differential rotation contours. However, in our two-zone spherical shell model set-up, a strongly varying latitudinal entropy gradient might be obtained self-consistently with a suitable background $d\bar{S}/dr$ profile. Indeed, this could result in stronger entropy gradient perturbations $\partial\langle S \rangle/\partial\theta$ in the thermally equilibrated state which could in turn lead to non-cylindrical differential rotation profiles. This topic will be addressed in future work.

We may attempt to provide some estimates on the solar value of the overshooting lengthscale using the results of our study. We note, however, that such extrapolations tend to be speculative to some degree as values of many parameters used here are very different from the solar ones. For instance, $Ra_{\odot} \sim O(10^{20})$ and $Pr_{\odot} \sim O(10^{-6})$ (e.g., [Ossendrijver 2003](#)), while our models operate in a much lower Ra and much higher Pr regime.

These caveats aside, we can use the scaling relationship between δ_G and the ratio of the densities R_{ρ} to estimate the solar overshoot depth. We consider the region of the convection zone spanning from the tachocline to the base of the granulation boundary layer ($r_o \approx 0.9983R_{\odot}$), a region characterized by 11 e-foldings in density (e.g., Model S; [Christensen-Dalsgaard et al. 1996](#)). Using this, and the values of the density at the base of the radiative zone at $r_i \approx 0.2R_{\odot}$ and at the base of the CZ at $r_c \approx 0.71R_{\odot}$, we find that $R_{\rho} \approx 0.003$. Based on our scaling of $\delta_G = 0.078R_{\rho}^{0.36}$ from Section 3, we estimate an overshoot lengthscale for the Sun of $\delta_G \approx 0.0097$ or, equivalently, $\delta = \delta_G r_o \approx 0.1H_p$, where $H_p \approx 5.7 \times 10^9 \text{ cm}$ is the pressure scale-height at the base of the solar CZ extracted from Model S. This estimated value for the solar overshoot lengthscale is similar to the estimates from other studies. For instance, [Brummell et al. \(2002\)](#) used 3D compressible simulations to estimate an overshoot depth in the range $0.02H_p - 0.11H_p$, while stellar

evolution models typically assume overshoot depth values of the order of $0.1H_p$. Helioseismic studies suggest that the upper limit for the solar overshoot depth is about $0.07H_p$ (see, e.g. [Monteiro et al. 1994](#)).

Carrying out a similar exercise based on Rossby number is more difficult as there is still no clear consensus on the value of deep solar convection’s Rossby number. Estimates of convective overturning time based on the B–V color index suggest that $\text{Ro}_\odot \sim 0.04$ ([Corsaro et al. 2021](#)), whereas [Featherstone & Hindman \(2016b\)](#) suggested that a value ≤ 0.01 was likely based on observed spatial scale of supergranulation. In principle, this parameter could be inferred for the Sun through helioseismic measurements of deep convection, but attempts to do so have led to inconsistent results (e.g., [Hanasoge et al. 2012](#); [Greer et al. 2015](#); [Nagashima et al. 2020](#)). Given these present uncertainties, we refrain from using the scaling law of δ_G with Ro to obtain estimates of the solar overshoot lengthscale. Alternative observational approaches, however, such as those based on inertial mode observations ([Gizon et al. 2021](#)) may shed further light on this issue in the future.

1 We thank Nic Brummell and Pascale Garaud for useful discussions on overshooting convection over the years. This
2 work was supported by NASA grant No. 80NSSC17K0008. LK acknowledges support from the George Ellery Hale
3 Post-Doctoral Fellowship and from NASA’s Early Career Investigator Program grant No. 80NSSC21K0455. NF
4 acknowledges funding from NASA grant No. 80NSSC20K0193. The authors acknowledge the NASA High-End-
5 Computing program for providing the computational resources without which the numerical simulations of this work
6 would not have been possible. This work utilized resources from the University of Colorado Boulder Research Com-
7 puting Group, which is supported by the National Science Foundation (awards ACI-1532235 and ACI-1532236), the
8 University of Colorado Boulder, and Colorado State University. The Rayleigh code has been developed with sup-
9 port by the National Science Foundation through the Computational Infrastructure for Geodynamics under grants
10 NSF-0949446 and NSF-1550901.

APPENDIX

A. POLYTROPIC BACKGROUND STATE IN THE CZ

Following the anelastic benchmark study of Jones et al. (2011), we define a polytropic background state in the CZ with

$$\bar{T} = \bar{T}_c z, \quad \bar{\rho} = \bar{\rho}_c z^n, \quad \bar{P} = \bar{P}_c z^{n+1}, \quad (\text{A1})$$

where n is the polytropic index, and where \bar{T}_c , $\bar{\rho}_c$, and \bar{P}_c is the value of \bar{T} , $\bar{\rho}$ and \bar{P} at the base of the CZ, respectively. Assuming that our polytrope satisfies the hydrostatic balance given by

$$\frac{\partial \bar{P}}{\partial r} = -\bar{\rho}g = -\frac{\bar{\rho}GM}{r^2}, \quad (\text{A2})$$

where G is the gravitational constant and M is the stellar mass and defining the number of density scale-heights in the CZ given by N_ρ , we find an expression for the function z

$$z = a + \frac{b}{r}, \quad (\text{A3})$$

where

$$a = \frac{fb}{r_c}, \quad b = \frac{2GM}{5(n+1)c_p\bar{T}_c}, \quad (\text{A4})$$

and where

$$f = \frac{(r_c/r_o) \exp(N_\rho/n) - 1}{1 - \exp(N_\rho/n)}. \quad (\text{A5})$$

REFERENCES

- Acevedo-Arreguin, L. A., Garaud, P., & Wood, T. S. 2013, MNRAS, 434, 720
- Anders, E. H., Vasil, G. M., Brown, B. P., & Korre, L. 2020, Physical Review Fluids, 5, 083501
- Augustson, K., Brun, A. S., Miesch, M., & Toomre, J. 2015, ApJ, 809, 149
- Augustson, K. C., Brown, B. P., Brun, A. S., Miesch, M. S., & Toomre, J. 2012, ApJ, 756, 169
- Augustson, K. C., Brun, A. S., & Toomre, J. 2016, ApJ, 829, 92
- Augustson, K. C., & Mathis, S. 2019, ApJ, 874, 83
- Baraffe, I., Pratt, J., Goffrey, T., et al. 2017, ApJL, 845, L6
- Braginsky, S. I., & Roberts, P. H. 1995, Geophysical and Astrophysical Fluid Dynamics, 79, 1
- Browning, M. K., Brun, A. S., & Toomre, J. 2004, ApJ, 601, 512
- Brummell, N. H., Clune, T. L., & Toomre, J. 2002, ApJ, 570, 825
- Brun, A. S., Browning, M. K., & Toomre, J. 2005, ApJ, 629, 461
- Brun, A. S., Miesch, M. S., & Toomre, J. 2004, ApJ, 614, 1073
- . 2011, ApJ, 742, 79
- Brun, A. S., Strugarek, A., Varela, J., et al. 2017, ApJ, 836, 192
- Calkins, M. A., Julien, K., & Marti, P. 2015, Proceedings of the Royal Society of London Series A, 471, 20140689
- Charbonneau, P., & MacGregor, K. B. 1997, ApJ, 486, 502
- Christensen-Dalsgaard, J., Dappen, W., Ajukov, S. V., et al. 1996, Science, 272, 1286
- Corsaro, E., Bonanno, A., Mathur, S., et al. 2021, A&A, 652, L2
- Dikpati, M., & Charbonneau, P. 1999, ApJ, 518, 508
- Elliott, J. R., Miesch, M. S., & Toomre, J. 2000, ApJ, 533, 546
- Featherstone, N. 2018, Geodynamics/Rayleigh: Bug-Fix-Release: 0.9.1, v0.9.1, Zenodo, doi: [10.5281/zenodo.1236565](https://doi.org/10.5281/zenodo.1236565)
- Featherstone, N. A., Browning, M. K., Brun, A. S., & Toomre, J. 2009, ApJ, 705, 1000
- Featherstone, N. A., & Hindman, B. W. 2016a, ApJ, 818, 32
- . 2016b, ApJL, 830, L15
- Featherstone, N. A., & Miesch, M. S. 2015, ApJ, 804, 67
- Garaud, P., & Acevedo Arreguin, L. 2009, ApJ, 704, 1
- Garaud, P., & Bodenheimer, P. 2010, ApJ, 719, 313
- Gastine, T., & Wicht, J. 2012, Icarus, 219, 428

- Gastine, T., Yadav, R. K., Morin, J., Reiners, A., & Wicht, J. 2014, *MNRAS*, 438, L76
- Ghizaru, M., Charbonneau, P., & Smolarkiewicz, P. K. 2010, *ApJL*, 715, L133
- Gilman, P. A., & Glatzmaier, G. A. 1981, *ApJS*, 45, 335
- Gizon, L., Cameron, R. H., Bekki, Y., et al. 2021, *A&A*, 652, L6
- Gough, D. O. 1969, *Journal of Atmospheric Sciences*, 26, 448
- Greer, B. J., Hindman, B. W., Featherstone, N. A., & Toomre, J. 2015, *ApJL*, 803, L17
- Guerrero, G., Smolarkiewicz, P. K., de Gouveia Dal Pino, E. M., Kosovichev, A. G., & Mansour, N. N. 2016, *ApJ*, 819, 104
- Guerrero, G., Smolarkiewicz, P. K., Kosovichev, A. G., & Mansour, N. N. 2013, *ApJ*, 779, 176
- Hanasoge, S. M., Duvall, T. L., & Sreenivasan, K. R. 2012, *Proceedings of the National Academy of Science*, 109, 11928
- Hotta, H. 2017, *ApJ*, 843, 52
- Howe, R. 2009, *Living Reviews in Solar Physics*, 6, 1
- Hurlburt, N. E., Toomre, J., & Massaguer, J. M. 1986, *ApJ*, 311, 563
- Hurlburt, N. E., Toomre, J., Massaguer, J. M., & Zahn, J.-P. 1994, *ApJ*, 421, 245
- Jones, C. A., Boronski, P., Brun, A. S., et al. 2011, *Icarus*, 216, 120
- Jones, C. A., Kuzanyan, K. M., & Mitchell, R. H. 2009, *Journal of Fluid Mechanics*, 634, 291
- Käpylä, P. J. 2019, *A&A*, 631, A122
- Käpylä, P. J., Rheinhardt, M., Brandenburg, A., et al. 2017, *ApJL*, 845, L23
- Käpylä, P. J., Viviani, M., Käpylä, M. J., Brandenburg, A., & Spada, F. 2019, *Geophysical and Astrophysical Fluid Dynamics*, 113, 149
- Kitchatinov, L. L., & Ruediger, G. 1995, *A&A*, 299, 446
- Korre, L., Brummell, N., & Garaud, P. 2017, *PhRvE*, 96, 033104
- Korre, L., Brummell, N., Garaud, P., & Guervilly, C. 2021, *MNRAS*, 503, 362
- Korre, L., Garaud, P., & Brummell, N. H. 2019, *MNRAS*, 484, 1220
- Lantz, S. R. 1992, PhD thesis, CORNELL UNIVERSITY.
- Latour, J., Spiegel, E. A., Toomre, J., & Zahn, J.-P. 1976, *ApJ*, 207, 233
- Latour, J., Toomre, J., & Zahn, J.-P. 1981, *ApJ*, 248, 1081
- Maeder, A. 1975, *A&A*, 40, 303
- Massaguer, J. M., Latour, J., Toomre, J., & Zahn, J.-P. 1984, *A&A*, 140, 1
- Matilsky, L. I., Hindman, B. W., & Toomre, J. 2020, *ApJ*, 898, 111
- Matsui, H., Heien, E., Aubert, J., et al. 2016, *Geochemistry, Geophysics, Geosystems*, 17, 1586
- McIntyre, M. E. 2007, in *The Solar Tachocline*, ed. D. W. Hughes, R. Rosner, & N. O. Weiss, 183
- Miesch, M. S., Brun, A. S., & Toomre, J. 2006, *ApJ*, 641, 618
- Miesch, M. S., & Hindman, B. W. 2011, *ApJ*, 743, 79
- Monteiro, M. J. P. F. G., Christensen-Dalsgaard, J., & Thompson, M. J. 1994, *A&A*, 283, 247
- Nagashima, K., Birch, A. C., Schou, J., Hindman, B. W., & Gizon, L. 2020, *A&A*, 633, A109
- Ossendrijver, M. 2003, *A&A Rv*, 11, 287
- Pal, P. S., Singh, H. P., Chan, K. L., & Srivastava, M. P. 2007, *Ap&SS*, 307, 399
- Parker, E. N. 1993, *ApJ*, 408, 707
- Pinsonneault, M. 1997, *ARA&A*, 35, 557
- Pratt, J., Baraffe, I., Goffrey, T., et al. 2017, *A&A*, 604, A125
- Racine, É., Charbonneau, P., Ghizaru, M., Bouchat, A., & Smolarkiewicz, P. K. 2011, *ApJ*, 735, 46
- Rempel, M. 2004, *ApJ*, 607, 1046
- . 2005, *ApJ*, 622, 1320
- . 2006, *ApJ*, 647, 662
- Renzini, A. 1987, *A&A*, 188, 49
- Rogers, T. M., & Glatzmaier, G. A. 2005, *ApJ*, 620, 432
- Rogers, T. M., Glatzmaier, G. A., & Jones, C. A. 2006, *ApJ*, 653, 765
- Ruediger, G. 1989, *Differential rotation and stellar convection*, Gordon & Breach, New York
- Shaviv, G., & Salpeter, E. E. 1973, *ApJ*, 184, 191
- Singh, H. P., Roxburgh, I. W., & Chan, K. L. 1998, *A&A*, 340, 178
- Tobias, S. M., Brummell, N. H., Clune, T. L., & Toomre, J. 2001, *ApJ*, 549, 1183
- Toomre, J., Zahn, J.-P., Latour, J., & Spiegel, E. A. 1976, *ApJ*, 207, 545
- Viviani, M., & Käpylä, M. J. 2021, *A&A*, 645, A141
- Wood, T. S., McCaslin, J. O., & Garaud, P. 2011, *ApJ*, 738, 47
- Zahn, J.-P. 1991, *A&A*, 252, 179
- Zahn, J. P., Toomre, J., & Latour, J. 1982, *Geophysical and Astrophysical Fluid Dynamics*, 22, 159